Paulo Filipe Valverde das Neves

Graduate in sciences of physics engineering

Building a Low-Cost AFM with a Quartz Sensor and its Advantages

Dissertation submitted in partial fulfillment
of the requirements for the degree of

Master of Science in
Physics Engineering

Supervisors: Ana Gomes Silva, Prof. Dr., Faculdade de Ciências e Tecnologia da Universidade Nova de Lisboa

Mário S. Rodrigues, Prof. Dr., Faculdade de Ciências da Universidade de Lisboa

Examination Committee

Chairperson:	Prof. Dr. Yuri Fonseca da Silva Nunes
Raporteur:	Prof. Dr. José Luís Constantino Ferreira
Member:	Prof. Dr. Mário Manuel Silveira Rodrigues

FACULDADE DE
CIÊNCIAS E TECNOLOGIA
UNIVERSIDADE NOVA DE LISBOA

September, 2017

Building a Low-Cost AFM with a Quartz Sensor and its Advantages

This document was created using the (pdf)LaTeX processor, based in the "unlthesis" template[1], developed at the Dep. Informática of FCT-NOVA [2].
[1] https://github.com/joaomlourenco/unlthesis [2] http://www.di.fct.unl.pt

Acknowledgements

I will start by thanking my supervisor Professor Ana G. Silva who brought focus to my abstract ideas, into the subject of AFM, where I learned about micro and nano manipulation, but also for informing me of the opportunity to work in the Atomic Force Microscopy Laboratory of the Physics department of Faculdade de Ciências da Universidade de Lisboa and promoting the interaction that later allowed me to do my work. The guidance and valuable suggestions also cannot be understated, as they helped me improve my work greatly. Of course, I would like to thank Professor Margarida Godinho and my supervisor Professor Mário Rodrigues for giving me the possibility of joining their research group and develop work, as well as learn, about such an interesting subject. More specifically, thanks to Professor Mário Rodrigues from whom I learned a lot, not only about the subject of my work but also about working with other people.

I am also very grateful to the members of the laboratory: Arthur Vieira, Miguel Vitorino for the discussions about the AFM system which allowed to make a better approach during the planning and design phase, and to Ana Carapeto for speeding up the process of acquiring a certain chemical substance.

Finally I would like to thank all of my family and specially my parents for all the support and care that allowed me to even able to study and be the person that I am today, I really can't express in words the gratitude that I feel towards them, for all they have done.

Abstract

Atomic Force Microscopy (AFM) and similar technologies are gaining extraordinary relevance thanks to their capabilities in manipulating on the micro and nano scale and performing studies with atomic resolution. From RoboticMicro-Assembly to pharmacology and cancerology the AFM technology is being applied and developed, however the instruments and equipment necessary to perform research are very expensive, which limits the development and use of this technology.

In this work, the first decisive stage for the construction of a low-cost AFM, with a tuning fork as a sensor was done. Its design and planning carefully considered economical options and a number of AFM components were made from scratch, using computer assisted design (CAD) software, 3D printing and other methods. This AFM has the notable characteristic of using a tuning fork as a sensor, which besides being a more cost-effective option, also brings more applications and advantages in relation to the traditional sensors used.

One of the benefits of the AFM is in the study of nano-mechanical properties, which can lead to a better understanding of deceases, biological processes or new construction materials, given the prevalence of this topic, the method for using an AFM with a tuning fork as a sensor, to study such properties, is studied and demonstrated. The value of the Young's modulus, is determined successfully for some samples and compared to the values found in literature with other methods.

Besides studying mechanical properties the custom made AFM is used to perform topography of calibration samples and CD samples, where pits and lands (encoded data) were observed, confirming that the AFM is functional. The quality of the AFM is not identical to that of an expensive commercial AFM and economical improvements for further development are suggested.

Keywords: Atomic Force Microscopy Development, Nano-mechanical Properties, Low-cost AFM, Contact Mechanics, Tuning Fork

Resumo

A Microscopia de Força Atómica e tecnologias semelhantes, têem ganho extraordinária relevância graças às suas capacidades em obter topografia com resolução atómica e manipular à micro e nano escala. A tecnologia MFA tem sido aplicada e desenvolvida desde a montagem micro-robótica até à farmacologia e cancerología, no entanto os instrumentos e equipamentos necessários para realizar investigação são bastante dispendiosos, o que é um factor limitante no estudo e desenvolvimento desta tecnologia.

Neste trabalho foi executada a primeira fase decisiva na construção de um microscópio de força atómica (MFA), de custo reduzido, usando um diapasão como sensor. O seu desenho e planeamento teve em consideração opções económicas e consequentemente vários componentes foram criados usando software de desenho assistido por computador, impressão a 3D e outros métodos. Uma das características de destaque deste MFA está no uso de um diapasão como sensor, o que para além de mais económico, também disponibiliza outras aplicações e vantagens em comparação com os sensores tradicionalmente usados.

Um dos benefícios do MFA é permitir o estudo de propriedades nano-mecânicas, que podem levar a um melhor entendimento de processos biológicos ou até novos materiais de construção. Considerando a importância deste tópico, o método para usar um MFA com um diapasão foi estudado e demonstrado. Inclusive, o valor do módulo de Young, foi determinado para algumas amostras e comparado com valores presentes na literatura, apresentando resultados dentro dos valores esperados.

Para além de ter sido usado para o estudo de propriedades nano-mecânicas, o MFA desenvolvido foi usado para obter imagens topográficas de amostras de calibração e de CDs, confirmando que o MFA está operacional. No entanto a qualidade deste MFA não é idêntica à de um MFA comercial e melhoramentos de baixo custo foram sugeridos para futuro desenvolvimento do instrumento.

Palavras-chave: Desenvolvimento Microscópio de Força Atómica, Propriedades Nano-mecânicas, MFA de Custo-eficiente, Contacto Mecânico, Diapasão

Contents

List of Figures

List of Tables

Acronyms

AFM	Atomic Force Microscopy.
CAD	Computer Aided Design.
DAC	Digital to Analogue Converter.
FIM	Field Ion Microscopy.
FWHM	Full Width at Half Maximum.
JKR	Johnson-Kendall-Roberts.
LER	Length Extensional Resonator.
PDMS	Poly-Di-Methyl-Siloxane.
PID	Proportional-Integral-Derivative.
PLL	Phase-Locked Loop.
PSD	Phase-Sensitive Detector.
STM	Scanning Tunnelling Microscopy.

Chapter 1

Introduction

1.1 AFM in present and future times

As the demand for more precise and efficient methods for studying and dealing with materials on the micro and nano scale, technologies such as Atomic Force Microscopy (AFM) gain extraordinary relevance. Mostly thanks to their capabilities in allowing to perform imaging with atomic resolution, as well as manipulation on the micro and nano scale. To continue developing new technologies in the future, it is important to be able to direct this technology to industrial applications, and to increase our understanding of processes at the nano level.

One very interesting field, as often occurs, related to both research and industry is the Robotic Micro-Assembly, for the development of this field new techniques are required as well as novel nanotechnologies that can be applied in an industrial context [1]. The AFM not only allows micro and nano visualization through topography but it is also capable of performing micro and nano manipulation, although its industrial application is thwart by some hindrances. Recently, there has been research and work that are successfully overcoming some of the inherent problems by using an AFM quartz crystal sensor [2], to make topography simultaneously with manipulation. This is especially relevant for this thesis as one of the objectives is the development of an AFM that uses a quartz crystal sensor, instead of an optical system.

There are other fields where AFM is being applied to, for example, pharmacology and cancerology which is tied to the pharmaceutical industries. In this context, the AFM is being used to perform topography and nanoindentation, so that the necessary information about the mechanical properties of certain cells may be acquired [3–5], furthermore it has also been used to manipulate individual cells, which allows studies that give information at the single cell level, making AFM an important tool to understand biological systems,

for example, recent developments enabled the use of cantilevers as nano-pipettes which were used for adhesion and injection on single cell level [6].

Another industry that is making use of the AFM technologies is the construction industry, more specifically on the study of cement materials. In this work [7], AFM was used to find the roughness of two different regions on a cement material. This allowed to choose a supplement for the cement, inferring certain required characteristics. Other uses of AFM in the construction industry can be found in this review [8].

While presenting some of the current applications of AFM technology, it is important to note these are just a few of the many applications and the present research on a topic that gained a lot of relevance over the last 20 years as can be shown in Figure 1.1, which gives the general tendency.

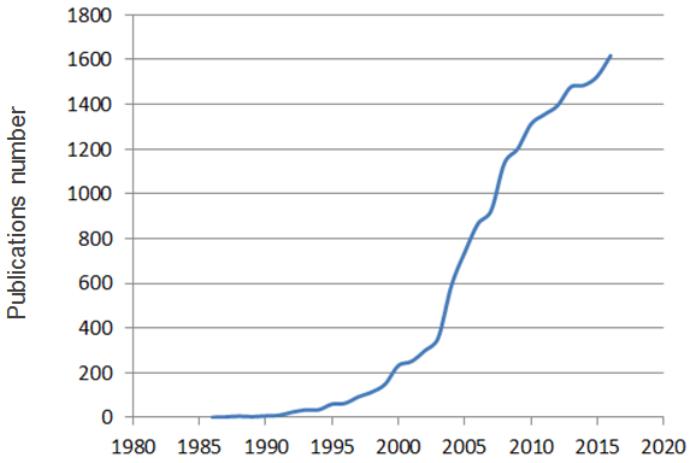

Figure 1.1: Number of papers published each year, the data was acquired from a Pubmed search using AFM.

Besides the construction of a quartz sensor AFM, the thesis will also be focused on the study of mechanical properties at the micro and nano level. Using nanoindentation techniques like the PeakForce QNM [9], but also novel techniques such as harmonic force microscopy [10], the AFM instrument it capable of successfully increasing our knowledge on complicated diseases, such as the Parkinson's disease [11] or Alzheimer's [12].

To use an AFM but specially to build one, it is necessary to be aware of the several subtleties of practical use, for that reason I took a 4-5 weeks "internship"in July of 2016 at the physics department of "Faculdade de Ciências da Universidade de Lisboa", to learn more in detail and to get comfortable with those subtleties of practical use. During this time I made topographic images of DNA plus protein (Haa) samples, an example can be seen in Figure 1.2. Presumably the curvilinear shape, being pointed by the arrow, corresponds to the DNA segment. In turn, the globular shape viewed in the figures seems to correspond to the protein attached to the DNA segment forming a complex.

In this experiment, the samples provided had a section of DNA previously amplified which means, to select the region of interest and expressed (production of several

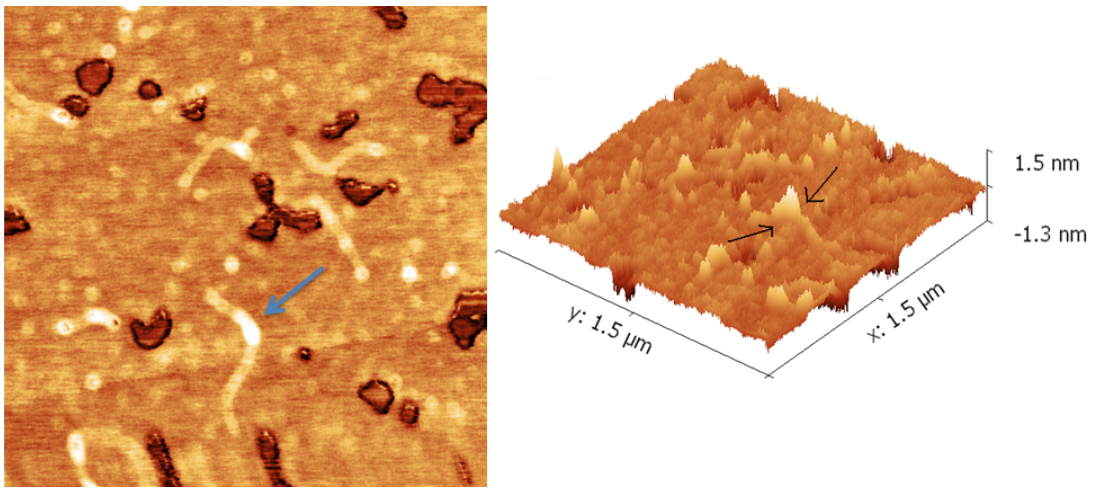

Figure 1.2: Topography of protein DNA complexes in 2D and 3D images, both with 1.5 μm on each side.

copies) with the intention of corroborating the formation of complexes (the binding interaction between DNA and the protein) visually. More specifically this protein, which was overproduced should form a complex at about one third of the DNA length.

This work was important to get some experience, although constructing an AFM with a different setup from scratch, while using a different type of sensor, was altogether a new challenge.

1.2 Brief theoretical review

To build an AFM, an understanding of the instrumentation and processes involved is needed, as well as knowledge on the forces involved in the tip-sample interactions. Furthermore, knowing what variables will be measured and how they will behave regarding different interactions, can be of great importance. This section was written to make a brief observation of the theoretical concepts in play.

An effective way to start discussing the theory concept behind the technology of an AFM, is by looking at the Lennard-Jones curve. Although this curve is incomplete, because it doesn't have the representation of all the interactions forces, it does represent the Van der Waals forces, as well as the Pauli repulsion, which are big contributors in defining the interaction both in long and short range respectively. When tip gets very close to the sample the atoms from the tip and sample start "competing"for space so the prevalent forces are the repulsive ones, as it can be seen in Figure 1.3, this is explained by theory as Pauli exclusion principle that said two or more identical fermions cannot occupy the same quantum state. Meaning that when the electrons of the tip start contacting the electrons of the sample the repulsive component defines the interaction. On the other hand, at further distances the attractive Van der Waals forces take a more key role in defining the interaction which has an attractive nature.

When the resulting force is whithin its attractive range, as well as the tip-sample distance is under a certain value, an incident called jump-to-contact can occur [13] (where the tip becomes attached to the sample), there are of course many other factors related to this incident, for example, tip stiffness and other forces, like the capillary forces.

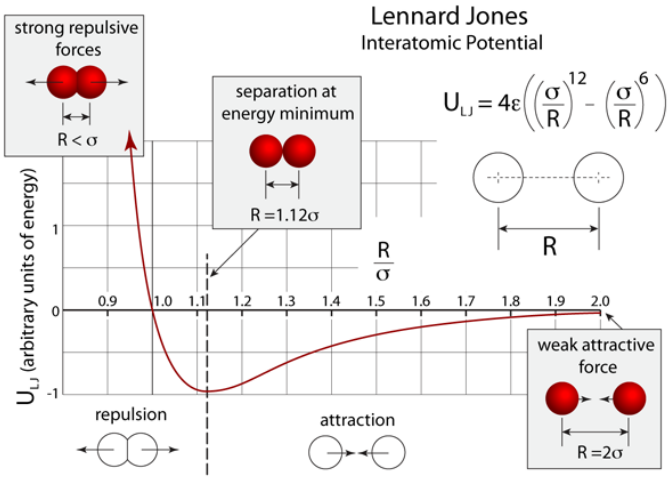

Figure 1.3: Plot of Lennard-Jones potential function, adapted from [14].

The forces involved in tip-sample interactions are:

- **Van der Waals Forces** - There are several forces that are considered Van der Waals Forces, such as the ones that come from the London dispersion which is the weakest. These are related to electrostatic interactions between two permanent charges in atoms or molecules.
- **Chemical Forces** - These occur when the tip is sharing electrons or exchanging electrons with the surface, if a chemical bond is formed it usually dominates the interaction.
- **Contact Forces** - Associated with the short range repulsive forces explained by the Pauli exclusion principle, but also with the electrostatic interaction between two charged particles.
- **Magnetic Forces** - These forces are considered a long-range interaction and they can be both attractive or repulsive forces.
- **Capillary Forces** - When there is a confined configuration at the nano scale the effect resultant from capillary condensation will be present [15]. This strong attractive force can cause discontinuities in the force-distance curves.
- **Viscosity Forces** - These forces are influenced by the cantilever's speed and geometry, as well as the sample surface viscosity [16]. Due to their low intensity at long range they are not so relevant in the attractive region but more at close range, in the repulsive region.

The variables that are being measured in a traditional AFM tapping mode, are the amplitude and phase of an oscillating cantilever. While the tip moves, the resulting force from the tip-sample interaction determines the amplitude and phase of the tip, that is oscillating near its resonant frequency. These variables are related to the excitation frequency as it can be seen in the following expressions 1.1 and 1.2, where γ is the damping constant, ω_{exc} the excitation frequency, k is the spring constant, m the mass of the cantilever and A_{exc} the amplitude of the oscillation of the cantilever when excited at ω_{exc}. The deduction and reasoning behind these equations are of paramount importance for the experimental work in this dissertation and they will be studied further ahead in section 4.1.

$$A = \frac{kA_{exc}}{\sqrt{(\omega_{exc}\gamma)^2 + \left(k - \omega_{exc}^2 m\right)^2}} \tag{1.1}$$

$$\varphi = \arctan\left(\frac{\omega_{exc}\gamma}{\omega_{exc}^2 m - k}\right) \tag{1.2}$$

The interaction changes the natural frequency of the system that goes from $\omega_0 = \sqrt{k/m}$ to $\omega_0 = \sqrt{(k+k_i)/m}$. If the interaction is attractive k_i will be negative and the resulting k smaller, which will create a resonance frequency shift, as the shift occurs but the excitation frequency remains the same, the amplitude for that specific frequency will be significantly different, as it can be observed in Figure 1.4.

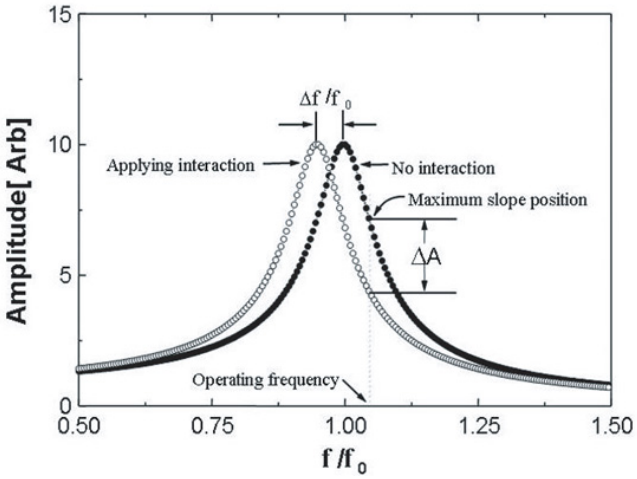

Figure 1.4: Natural frequency shift and its implications in amplitude, adapted from [17].

The amplitude is not the only variable that will change as the resonance frequency changes, the phase will also suffer a significant variation much like the amplitude as it can be seen in Figure 1.5.

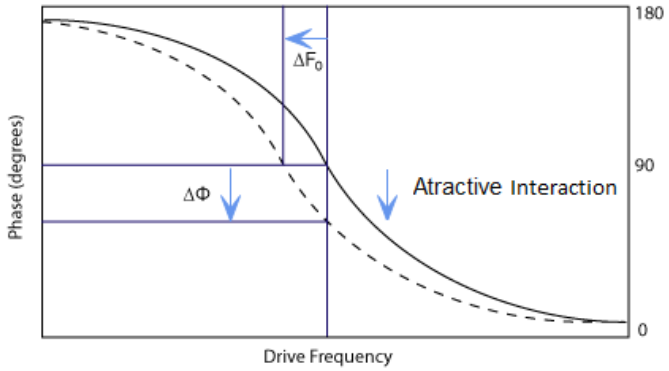

Figure 1.5: Frequency shift in attractive interactions and its implications in phase, adapted from [18].

1.3 Advantages and disadvantages of a quartz crystal sensor AFM

What follows is a summary on the advantages of using a quartz crystal sensor AFM in comparison to a commercial AFM, based in literature. Since this AFM doesn't require an optical system, it inherently avoids problems where the radiance from the diode can be affected by outside light. In the early 2000s, the diode laser was also being a factor in increasing thermal drift and noise from thermal mode hopping which was the limiting source of noise [19]. Although presently it is not as problematic as before, it still adds thermal noise to the system.

Besides requiring less instrumentation, the quartz crystal sensors are also cheap in comparison with the commercial cantilevers. Another great advantage is the non-contact approach, which helps preventing tip and sample damage, something that is particularly useful when dealing with fragile biological samples [20].

To achieve extremely high resolution, high vacuum and low temperature (4.2K) is necessary, which often comes with complex cooling and pumping systems to achieve said vacuum and low temperature. In this type of set up the simplicity of the quartz crystal sensor AFM presents, is a big advantage. Which is why quartz crystal sensor AFM is seeing increase use in high resolution low temperature (LT), ultra-high vacuum (UHV) AFM [21]. Figure 1.6 adapted from article [22], presents the image of a molecule, acquired with one of these high resolution AFMs while using a tuning fork as a sensor in a *Qplus* configuration.

Yet another advantage of the tuning fork is that, since it is very stiff, it also avoids jump-to-contact, which is an incident that has many unfavourable implications in AFM studies. The cantilevers from traditional AFMs have to be soft enough to deflect, but this means that when doing nano indentations it is hard to know how much of the signal is indentation and how much is deflection, which is a problem the tuning fork does not have.

On the side of the disadvantages, there has not been reported a quartz crystal sensor

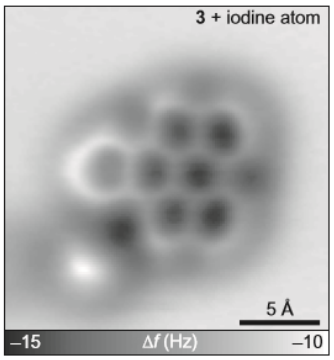

Figure 1.6: High-resolution AFM topographic image of Diisononyl phthalate adapted from article [22].

capable of performing very high-speed imaging, where the time per frame on a 250 nm scan range is close to 45 milliseconds [23]. This order of magnitude in time is necessary to study bio-molecular processes that can occur in milliseconds, which means a quartz crystal sensor AFM cannot observe some of the reactions in real time, but only the final result or the average state just like a common commercial AFM.

Besides speed, one of the minor inconveniences of using a quartz sensor AFM, is that the tips should be constructed and prepared for that specific sensor. However, this is not very problematic, as it will be discussed in section 3.4.

CHAPTER 2

STATE OF THE ART

2.1 Instrumentation

Unlike the laser based AFM, the quartz sensor AFM doesn't require an optical system. Instead of a laser and a photo sensor, it uses a quartz crystal that can be used as a sensor and an actuator. The initial AFMs with such a setup used a quartz tuning fork, and presented a noise level equal to the laser-based AFMs produced at the same time [19].

While the optical-deflection based AFM uses a Proportional-Integral-Derivative (PID) controller, with the function of stabilizing the distance between the tip and sample, the quartz sensor AFM can use a Phase-Locked Loop (PLL) controller in addition to the PID. This system allows to stabilize the phase of the input signal by maintaining the phase of the output signal correlated to the "initial phase"in a loop. A simplified scheme of the components used in the AFM previously described can be observed in Figure 2.1.

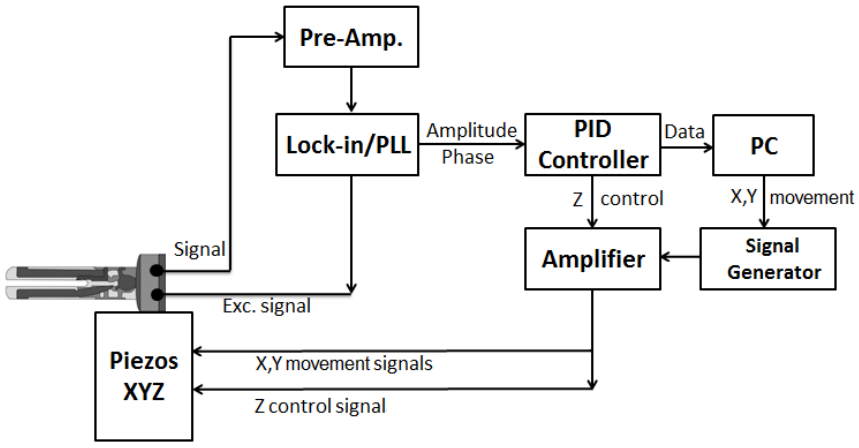

Figure 2.1: Scheme of the AFM components, with a tuning fork being excited.

The quartz crystal can act as an actuator by exciting it with a drive signal, which can be called input signal, and thus moving the tip attached to one of the crystal's prongs. In the loop system this drive signal is influenced by the response of the tip, which is the output signal of the crystal/sensor. By monitoring the phase of the drive signal and the output signal's phase in a loop with a Phase-Sensitive Detector (PSD) and maintaining their correlation the PLL is achieved [19].

The use of PLL in AFM emerged in 1997, and a few years later AFMs using quartz sensors expanded to studies in vacuum where atomic resolution is easier to achieve. This article reports the first atomic resolution attained with an AFM quartz sensor [24], it also introduces a few important improvements that quickly became popular, one of the most important would be the "QPlus"configuration, where one of the prongs of the fork is held fixed, as it can be observed in Figure 2.2. That wasn't the only configuration that improved the results though, the Length Extensional Resonator (LER), was another quartz sensor AFM that achieved atomic resolution, also known as the "needle sensor".

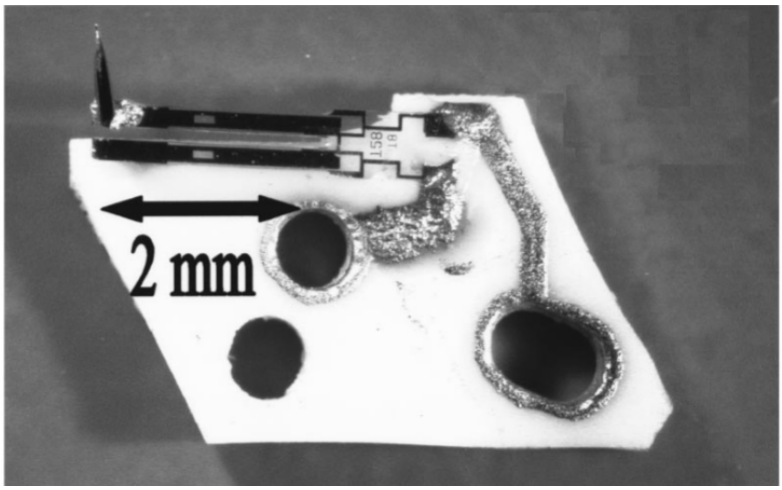

Figure 2.2: Photograph of the Qplus configuration [24].

One component that both the quartz sensor AFM and the traditional AFM requires, is the transimpedance pre-amplifier or in some cases a charge amplifier. In the most common AFMs it might even require several pre-amplifiers for each quadrant of the photo sensor.

In the case of the quartz sensor AFM it needs a pre-amplifier because the quartz crystal acts like a sponge, when it "contracts"it sends electrons, and when it "expands"it "pulls"electrons, what this means is that while acting as a sensor the quartz crystal will send a very small electric signal that needs to be converted with a gain to voltage. The transimpedance pre-amplifier is responsible for making this conversion and amplification, although simple, this component requires attentive planning. The transimpedance pre-amplifier is responsible for the magnitude of the output signal (after amplification) but also for the addition of noise during said amplification. Article [25] compares the use of a charge amplifier to a transimpedance pre-amplifier and shows that for higher operating

frequencies, like the ones used with LER the charge amplifier presents less noise than the transimpedance pre-amplifier. These are the type of considerations that will be taken into account when choosing the components.

Fast-forwarding to the beginning of 2013 it was reported an AFM quartz crystal sensor [2], with an imaging speed 5 times faster than that of a traditional AFM machine, one of the big differences between this one and the previously mentioned, is that instead of using a fork shaped sensor, cylindrical quartz crystal was used with a resonant frequency of approximately 3.58 MHz, where a tungsten tip will be glued, it is notable that this tip is much larger (millimeter size) than the ones commonly used (micrometer size), this allows an easier integration with a manipulation system, so that manipulation and imaging can be done simultaneously, as well as different sample access approaches.

2.2 Techniques for the study of nano-mechanical properties

As discussed in chapter 1.1, knowing the nano-mechanical properties of the materials, is important in several subjects from biology to the study of cement materials.

There are several techniques for the study of nano-mechanical properties, but most can be associated with one of three techniques. The first AFM technique to produce results in the search of mechanical properties was the Force-Volume [26, 27] now evolved and known as nanoindentation, this improved version is still being used recently for AFM-based diagnostics research at the cellular level [28]. The other branches are the Multifrequency and the Peakforce. Despite the appearance of the Multifrequency and the Peakforce being in response to some limitations of the Force-Volume there's certain aspects there are common to all. All these techniques revolve around getting force-curves, also known as force-distance curves, to which a mathematical model will be applied.

At the present time, the most used model to find the Young's modulus (from where the mechanical properties will be deduced) in a material, is the Hertzian contact model [29], which will be analysed and discussed in chapter 4.

Even though nano-indentation is widely used, there were other techniques that appeared in response to the Force-Volume limitations and that are regularly used, such as the Multifrequency or the HarmonicForce technique. To briefly describe this technique, it starts with the rough approximation, that the cantilever and tip can be considered a simple oscillator where position can be described by the expression 2.1, where z_0 is the always present static component, A the amplitude of oscillation and ϕ the phase shift.

$$z = z_0 + A\cos(\omega t - \phi) \tag{2.1}$$

Making a more precise description of the system, the harmonics induced by non-linearity effects must be taken into account, in addition, since the a tip is attached to the cantilever, eigenmodes must be considered [30]. Making the full expression the following 2.2, where the deflection z is a sum of all the eigenmodes contributions, nω the

frequency of the high-frequency components (Harmonics) and A_n the amplitude of each contribution.

$$z = z_0 + \sum_{n=1}^{N} A_n \cos(n\omega t - \phi_n) \tag{2.2}$$

By considering the information given by several modes, the multifrequency technique can work at much higher operation frequencies than Force-Volume, while still considering the non-linearity effects.

In this dissertation, the technique used is nanoindentation, so its procedure will now be described. The first step to perform nanoindentation is to determine and find the region that one intends to study, to this effect, a normal microscope or AFM imaging can be used. The tip should be placed above said region and a trigger-value must be defined, this can either be the target value of the indentation depth or a limiting amplitude value to signal the end of the measurement. The tip will approach the sample until the trigger points are achieved, by which point the tip stops, the distance is registered and the tip will retract. During the tip movement, the "force"is constantly being recorded, which will provide the distance-force curve. A good example to show and discuss a generic distance-force curve is shown in Figure 2.3. In this figure is possible to observe the previously mentioned jump-to-contact effect from the point 1 to point 2, then as the Z height decreases, there is an increase in tip deflection, the tip is then under the effect of adhesion, which is why there's a jump from point 4 to point 5 where the force is sufficient to release the tip.

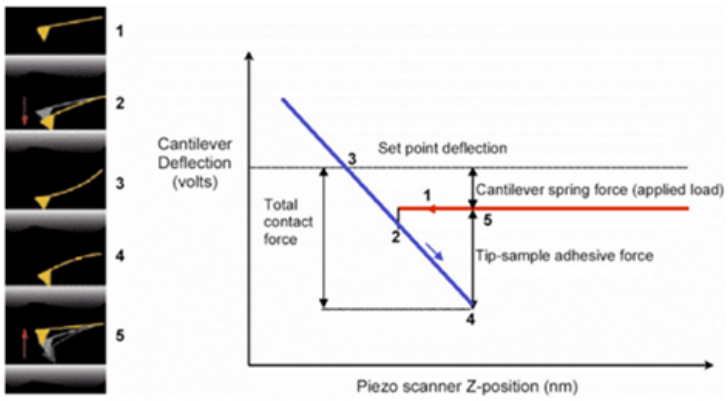

Figure 2.3: Example of a force-distance curve [31].

The main problem with the first method of nanoindentation, Force-Volume, was time and spatial resolution. The operation frequency was between 0.5 Hz to 10 Hz per pixel [32], and the control signal for the Z position of the tip was triangular which meant that if a higher operation frequency was used there would start occurring irregularities caused by resonance effects originated by the inflection points of the triangular signal.

Because of these limitations new techniques like the PeakForce were developed. The Figure 2.4 shows the evolution in ramp frequency or operation frequency from Force-Volume to PeakForce.

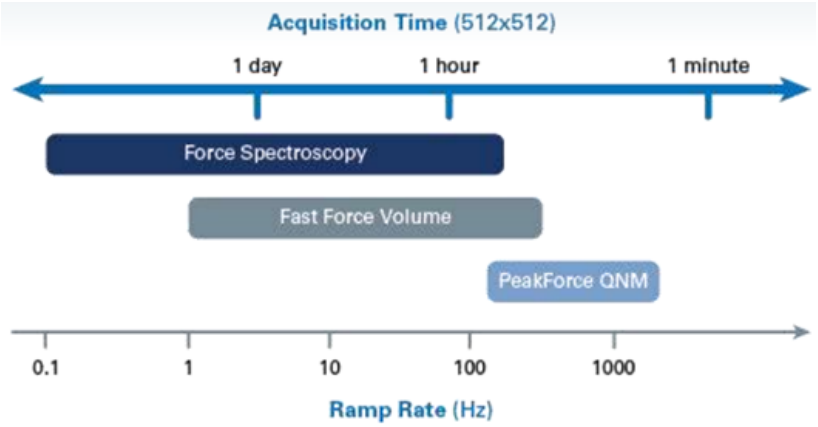

Figure 2.4: Comparison between the acquisition times of Force Volume and PeakForce [31].

By having a much higher ramp frequency the Peakforce technique gains advantageous similarities to the topography technique tapping mode, which is not affected by lateral forces, providing a higher resolution. However, in contrast with tapping mode, the PeakForce doesn't use frequencies close to the resonance frequency and by doing so, it avoids the necessity to use filters that often are needed in dynamic resonant systems. In practical terms, this means there must be special attention in knowing the resonance frequency of the system to guarantee that there will not be interference with the operation frequency. The main difference between PeakForce and Force-Volume is the operation signal, which allows the PeakForce ramp frequency to be higher. Instead of a triangular signal that can cause resonance effects, the PeakForce uses a sinusoidal signal with smoother inflection points, where resonance effects will be smaller.

Chapter 3

Project and Design of the AFM

The method employed in the development of this dissertation, was based in breaking down the main objective into many smaller and more manageable ones, and then defining the necessities and constraints applied to each one of them. The focus of this dissertation was the construction of a low-cost AFM based on a quartz crystal sensor, capable of operating at the same or higher level than a commercial AFM, this should be done by integrating components already available, while developing the others.

As a set goal, the AFM should have the capacity to move 30 micrometer on the X and Y axis, since this allows the observation of cells, which are usually the biggest subjects of interest to study with an AFM. Furthermore, it should have a range of 10 micrometer on the Z axis, to cover the respective height of the subjects of interest. One of the other features that the AFM is expected to have, besides being able to use a quartz crystal sensor, is to incorporate the traditional beam deflection sensor through the use of a cantilever and laser, however, in this work the implementation of such a system will not be discussed. Finally, all design decisions and incorporation of electrical components should try to pursue an economical use of the resources available.

To design and have a visual support for the planning of the AFM, Computer Aided Design (CAD) was used, more specifically the software *SolidWorks*.

3.1 Choosing the tuning fork

Choosing the right quartz crystal sensor is of critical importance in the quality of the acquired signal and the first decision to be made, was choosing between using a length extensional resonator (LER), or a tuning fork, which can be observed in Figure 3.1.

Both sensors operate with the same principles. Since they have quartz crystal and electrodes that will collect the charge produced when the sensor suffers a certain strain. Also,

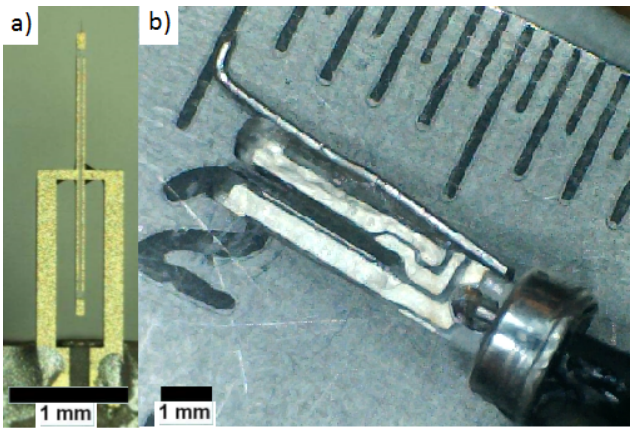

Figure 3.1: a) Length extensional resonator [25]. b) Tuning fork with a ruler on the background.

much like the tuning fork, when one prong of the LER moves the other prong moves as well, maintaining the center of mass position constant. In this work, the tuning fork is the most appropriate sensor, because it is more accessible as it is mass produced for watches and can be acquired for a low price. This has extra value in the AFM industry, because the sensors are usually very fragile and expensive. It is still notable that despite being very cheap, the tuning forks are still very sensitive and can achieve atomic resolution just like the LER, as mentioned in section 2.1.

There are several tuning forks with different shapes and sizes, which meant a detailed analyzes was needed to determine, which of the available tuning forks on the market would be the most appropriate for AFM. Defining the equation that would allow to calculate the expected sensitivity of each tuning fork is not trivial, so given the time constrains inherent to a dissertation a qualitative approach was preferred instead of a quantitative one.

In the article [24], Giessibl presents the expression 3.1 for the sensitivity S of a tuning fork in the *QPlus* configuration. Where d_{21} is the piezoelectric coupling constant for quartz, L_e the length of the electrode, L the length of the prong and t the thickness of the prong. If a rectangular parallelepiped shape is assumed for the prong, then K the spring constant of the prong is given by the expression 3.2 as found in article [33].

$$S = 12 d_{21} K \frac{L_e(L - \frac{L_e}{2}))}{t^2} \tag{3.1}$$

$$K = \frac{E w t^3}{4L^3} \tag{3.2}$$

Since the expression 3.1 was deduced for one prong of the tuning fork, because in *Qplus* the other prong is immobilized, it will not make for an accurate quantitative evaluation of a tuning fork with two prongs. However, the sensitivity or in other words, the charge generated by a strain in one prong, is the same. The only difference, is that in the normal configuration of the tuning fork, both prongs are moving, and by doing so,

have an additional signal source. What this means, is that although we can't calculate the true sensitivity of a tuning fork with this method, it is still possible to compare the sensitivities generated by the interaction with the sample using the equation 3.1. The signal-to-noise ratio is another factor important to consider, and the main noise sources at ambient temperature, are the thermal detector noise and the oscillator noise [25].

To calculate the sensitivity with the expression previously presented the tuning forks dimensions and K are needed, and since the K for two coupled prongs is very different from the K of one prong the expression 3.2 shouldn't be used. Many approaches were considered to calculate the tuning fork's spring constant, and after reviewing the literature many discrepancies were found. Discrepancies such as, while some articles report that the cantilever model minimizes the true spring constant [34], others find it, overestimates it [35] and there were others incoherencies that were also noted and reported in article [36]. However, something that the last three cited articles have in common, alongside most of, if not all the scientific community, that publishes on this subject, is the consensus around the *Cleveland Method* which allows to calculate the effective spring constant after adding a small mass on the tip of a micro cantilever [37]. Despite its accuracy this method required for a new experiment to be made with each of the tuning forks, and since there were time constraints as well as this being a qualitative approach another method was selected.

The method selected is called the *Geometrical Method* and it was presented in [36], where it was compared to the *Cleveland Method*, and found to have an 8.7 percent discrepancy, for a tuning fork with a resonance frequency of 32kHz. Given how different the values were expected to be, this level of error would not impact the qualitative comparison of the tuning fork's propensity for being used as an AFM sensor, and as such, it was the one employed. The expression presented in the article for the method was 3.3, where f_0 is the resonant frequency of the sensor, E is the Young's modulus of the quartz and ρ its density, while w is the width and t the thickness of the tuning fork's prongs.

$$K = 7.66w\left(E\rho^3\right)^{\frac{1}{4}}(tf_0)^{\frac{3}{2}} \tag{3.3}$$

With this equation, the K of the big and small tuning forks were calculated, these values are presented in table 3.1. Also presented in the table is the K value of the *Qplus* sensor of Giessibl for reference. The Rodrigues 2010 was already available at the laboratory, while the large tuning fork (DS 26 from microcrystal switzerland) and the small turning fork (DS 10 from microcrystal switzerland) were purchased and have their datasheet available online.

Now all the values necessary to calculate the sensitivity are available. However as reported in article [25], the figure of merit for a sensor is not just the sensitivity, but the k and resonance frequency also have to be taken into account, because the thermal noise in force gradient increases with k as shown in expression 3.4.

Table 3.1: Table with the dimensions and constant springs of four different tuning forks.

Tuning Fork	K (N/m)	f_0 (Hz)	L (μm)	L_e (μm)	t (μm)	ω (μm)
Giessibl 2011	1800	32768	2400	1600	214	126
Rodrigues 2010	42000	32768	6050	3740	600	340
Big T. Fork	52440	32768	6455	3990	640	365
Small T. Fork	15980	32768	4030	2490	400	225

$$\delta k_{thermal} = \sqrt{\frac{4kK_bTB}{\pi A^2 f_0 Q}} \tag{3.4}$$

Where K_bT is the thermal energy, A the amplitude, and B the bandwidth which is dependent on the component that will amplify the tuning fork signal, and for the purposes of being able to compare the results of this theoretical study with the results of Giessibl in [25] the same value of 1 Hz was assumed, throughout all calculations of this section.

Even though less impactful at ambient temperature than the thermal noise the oscillator noise must also be considered and its expression is present in 3.5, where n_{amp}, refers to the noise density of the pre-amplifier.

$$\delta k_{ocs} = \sqrt{2}\frac{K n_{amp}}{QS}\frac{\sqrt{B}}{A} \tag{3.5}$$

As expected the sensitivity, or charge generated by a certain deflection gets bigger as the electrodes on the tuning forks get bigger as well. However, having a larger size also means the sensors will be stiffer which increases all noise sources, but something else needs to be considered, the larger the mass of the tuning forks, the smaller the impact of adding an extra mass to the tip will be. When they are inside their capsules the tuning forks have approximately a Q factor of 50000, but once outside it lowers to approximately 4000, and then, the added tip will lower the Q factor of the sensors again. It was measured a decrease to approximately 1100 in the case of the larger tuning fork, while the smaller tuning fork displayed a decrease to 900. It is important to note the change in the Q factor will depend on tip mass, glue mass and other factors, so without a thorough control of said factors, these values can only be used in a qualitative comparison of the tuning forks. In the table 3.2 the tuning fork with the Qplus configuration was placed for reference, when comparing it to the other it is important to note that although the Qplus tuning fork, has one prong glued, thus lowering its Q factor, the quality factor is then artificially increased through a control loop. This means that when all the tuning forks present have a tip glued to them, the Qplus tuning fork will have a Q factor approximately three times bigger than the others, which will contribute to lower noise values.

The values for the thermal noise and oscillator noise calculated in table 3.2, are given per $\sqrt{Hz}$, the n_{amp} is not dependant on the tuning forks but on the amplifier, so for the purposes of these calculations the amplifier *FEMTO* was assumed for all, meaning the

Table 3.2: Table comparing some characteristics of four different tuning forks.

Tuning Fork	Sensitivity (μC/N)	Thermal N. (mN/m)	Oscillator N. (mN/m)
Giessibl 2011	2.80	3.1	0.27
Rodrigues 2010	50.60	25.6	1.05
Big T. Fork	63.12	27.7	0.96
Small T. Fork	19.19	16.9	1.17

n_{amp} was 90 $\frac{zC}{\sqrt{Hz}}$ [38]. In the calculations, an amplitude of 100pm was also assumed in other to stay coherent with the calculations of [25] so that a comparison could be made.

3.2 Design - Scanner

When building an AFM, the scanner is one of the most challenging parts, not only will it play a big role on the AFM operations and data quality, it was also one of the most complex individual pieces built.

An AFM requires the ability of moving the tip with high accuracy in relation to the sample and the scanner is the piece that will allow the AFM to move or excite the sample, with sub-nanometric precision, and for this AFM it should do so within a range of at least 30μm. When building such a system there are some basic decisions that have to be made. Should the sample move on the X, Y and Z axis while the tip remains in place, or should the tip move while the sample stays still? Besides that, there is a lot to consider between geometrically amplifying the movement, considering costs and other factors that will soon be discussed. As such, this was an iterative process and distinct designs were considered before landing on the final one. Since each have their merit, is it worthy to discuss all of them.

3.2.1 Amplified cylindrical scanner

The design for an amplified cylindrical scanner was the first to be considered, and emerged with the purposed of achieving the quality of a normal scanner at very low cost. In this design the movement on the X, Y and Z axis would be done from the sample, that would be placed on the scanner. To make the movement three piezoelectric actuators would be used in the set up roughly described in Figure 3.2.

To make a movement on the Z axis, all piezoelectric actuators simply had to expand and displace the cylinder upwards. At first sight, it might seem unnatural to think of deforming the scanner to achieve displacement, but actually the full displacement equates to 0.01% of the scanner length in this case.

In this scanner, the movement on the X and Y axis is not trivial, since to move the sample in one direction the cylinder tilts to one side, which corresponds to a movement in all three directions. This means that to achieve displacement in only X or Y the other

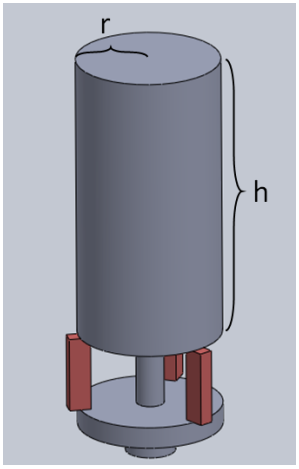

Figure 3.2: Rough design of the amplified cylindrical scanner.

actuators would have to compensate the undesired movement, which was a a disadvantage.

On the other hand this system presented a geometric amplification equal to $\frac{h}{r}$, because when the actuators expanded, xμm the top of the cylinder would move $\frac{h}{r}$ times more. A considerable advantage since it allows not only to buy smaller actuators which are less expensive, but also to control the natural gain by assembling a different cylinder with a different h r proportion. However, the system's low cost does not make up for its disadvantages, since a commercial scanner is so expensive that the purchase of small or large actuators, are both economical options in comparison.

3.2.2 Not amplified alfa scanner

Buying a micro-positioning system that could be controlled from the computer, was something to consider, since it is able to make large yet precise adjustments to the scanner position, unfortunately it was an expensive system and in the end we opted to go for a micro metric table already available in the laboratory. This table brought the first design constraints to the scanner, and allowed for a more definitive architecture to be planned, regarding the size and shape. This architecture would have to be assembled onto the micro metric table, and preferably have similar dimension, and since there was no geometrical amplification the actuators would need a length around 30mm to be able to cause displacements of 30μm as previously planned. In Figure 3.4, a solution for the requirements mentioned above is presented, and its design will now be discussed. Before though, it is worth mentioning that the piezoelectric actuators we settled on to make the displacement in the X and Y axis, were the *PK2JUP2 piezoelectric stack* from *Thorlabs*.

In opposite to the cylindrical scanner this scanner is not geometrically amplified, meaning that the displacement in the actuators will be equal to the displacement of the sample. The basic description of its operation would be, two actuators expand and contract, with high resolution steps, under a force load and by doing so displace a cube

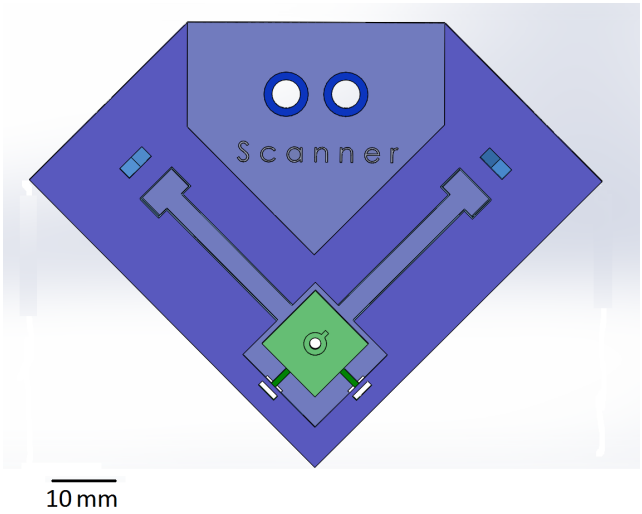

Figure 3.3: Top view of the not amplified scanner.

connected to the sample holder. Firstly, the structure has to be secured to the micro metric table and to that end, two screw holes concentric to the table's holes were made, they can be found above the word scanner in Figure 3.4. As mentioned before stability is key, and after screwing the scanner to the table with this two holes the scanner has no movement liberty.

To function properly, the actuators have to be under a certain load, and that load is secured on this scanner through a screw that goes against each actuator, compressing the actuators against the sample-holder-adapter on the scanner (represented in green). Naturally it is intended that when the actuators move, only the sample-holder-adapter moves, otherwise some of the 30μm required displacement would spread out in other regions of the scanner, that are not connected to the sample, meaning the sample wouldn't be able move the intended distance. The implications that arise from here, are that one end of the actuators needs to rest on a very stiff wall, in comparison to the other end, that should rests on a cube with two flexible bars connected to it, called flexures. Since according to the third Newton law the actuator will push the screw back, which in its stead is screwed to the nut, the region behind the nut hole has to be stiff, or in this case, thick enough to assure the displacement will be done by the cube.

As it is visible in Figure 3.4, the scanner has features that allow it to safely and easily incorporate the piezoelectric actuators and its supply cables, which are presented in Figure 3.5.

It is important to note that the screws need to be very well centered with the piezoelectric actuators, and have its points flattened to guarantee that there won't be bending forces that might jeopardize the actuators. Naturally the applied load has to have the same direction as the actuator's axis of displacement, meaning that the screw holes were centered with the actuators base.

The sample-holder-adapter is joint to the dark green flexures. The scaling and design

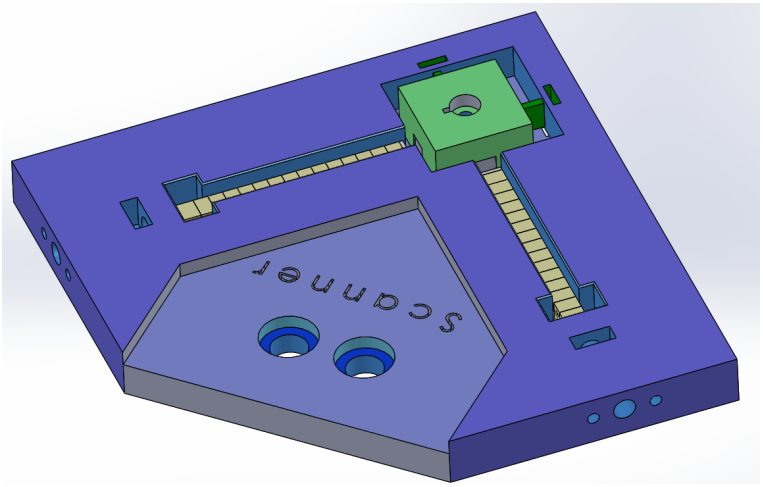

Figure 3.4: Oblique view of the not amplified scanner.

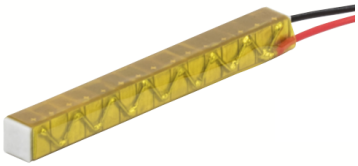

Figure 3.5: Thirty-centimeter-long piezoelectric stack used in the scanner for movement in the X and Y axis.

of these and other flexures, involve a lot of work and theory, furthermore, the process in which they were calculated is important to apply ideal load to the actuators, as it will be discussed in subsection 3.2.5. As such, the work related to the flexures, was compiled into one place and can be found in subsection 3.2.4.

The scanner was also designed so that the sample holders could be fastened to the scanner, and it accounts for the actuators movement, so that they wont slide out of position during operation.

Relative to the cylindrical scanner, this scanner has the advantage of not requiring additional electronic. However it still presented a disadvantage, the two axis movement were coupled, meaning that as one actuator moved and the cube position altered, the other actuator wouldn't be under the initially set conditions and the same could be said for the flexors. Although their maximum movement is 30μm, meaning the geometrical implications of that movement might not be relevant, but since a scanner main focus should be precision, we made improvements and designed the scanner that will be presented next.

3.2.3 Not amplified beta scanner

This architecture for this scanner is the culmination of all the precautions and issues discussed previously, although its design might be hard to understand at first, an above

side view can be seen in Figure 3.6.

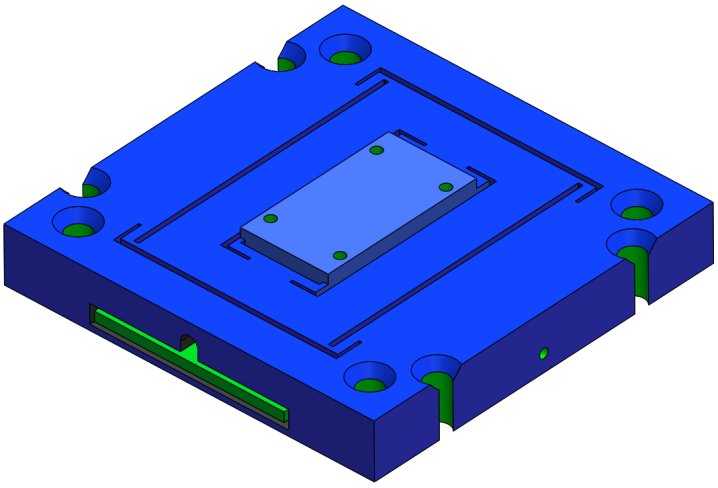

Figure 3.6: Above side view of this scanner iteration.

This scanner has several features, such as, eight tubes to screw the scanner on the micro metric table, an extruded center to place the sample holder, with four nut holes and screw tubes to fasten it, to mention some. The more important features would be the eight flexures, four for each axial movement and finally two weakened side structures, represented in green. Some of these features are best seen in the under side view of the scanner, shown in Figure 3.7, where the piezoelectric actuators are set in place.

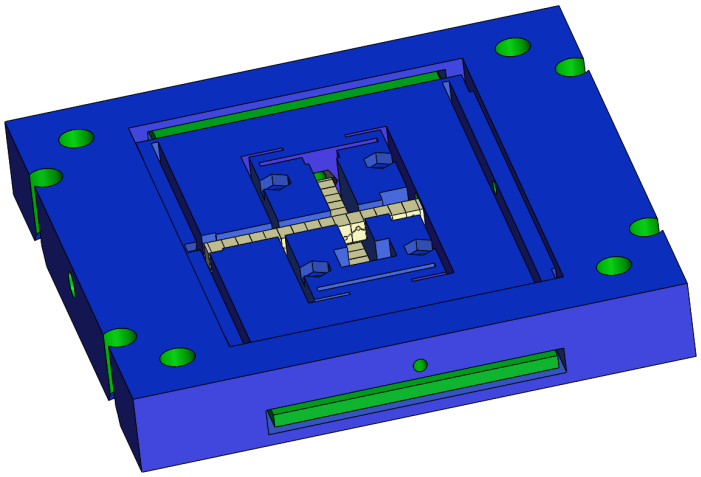

Figure 3.7: Bellow side view of the last scanner iteration.

As it is possible to observe, the actuators are set on different levels and they will ultimately move different parts of the scanner. As mentioned before, the problem with the first scanner not amplified, was that the movement on both axis was coupled, and the architecture of this scanner prevents that. Figure 3.8 was made to explain why that is, and how the scanner moves. The scanner is divided in three layers, the outer shell, the inner shell and the central block. The outer shell in itself never moves during scanning,

in its stead the inner shell moves in one direction, as represented by the brown arrows. When the actuator expands, one tip will be against the outer shell that is thick and stiff, while the other tip will push against a wall of the inner shell, this wall is also very stiff and its bending is negligible, on the other hand the four flexures are soft by comparison and will bend under the force represented by the other four brown arrows. Since the green structures coming out of the side of the second shell are not connected to the outer shell, both the inner shell and central block will move without any alteration on the central block flexures. Speaking of which, when the actuator with the black arrows expands, one tip will pushes against the inner shell and the other against a wall of the central block meaning once again, that the stiff walls will have negligible bending and that the flexures to where the black arrows are pointing will be the ones to bend.

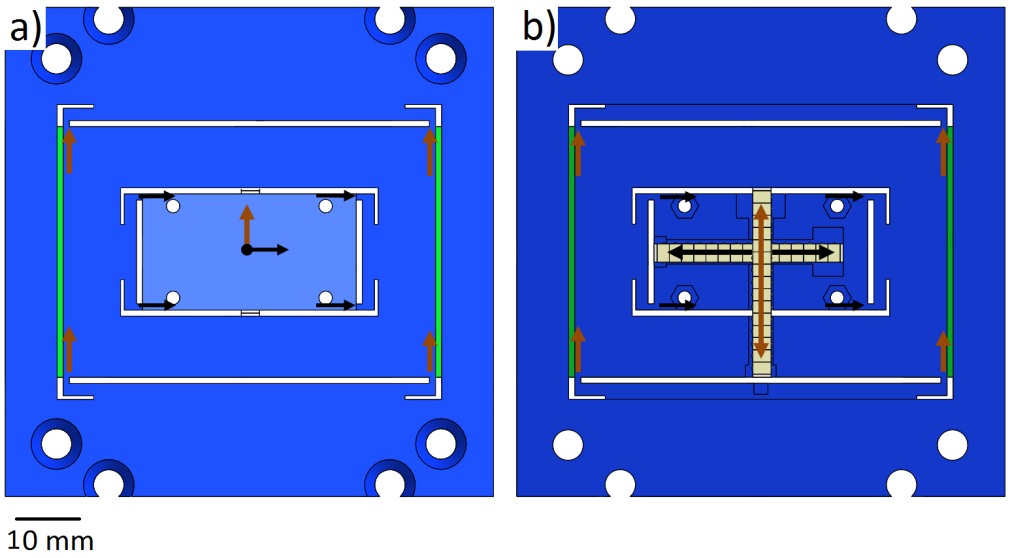

Figure 3.8: a)Top view of the scanner with arrows showing how the center moves in relation to each actuator. b)Bottom view of the scanner with same indicators.

This scanner's architecture allows it to make use of the micro metric table the laboratory already had, which was capable of a movement of 30μm in each direction, with minimal steps similar to a commercial one, but for one tenth of the cost it would take to buy one.

3.2.4 Euler-Bernoulli and flexures calculations

The theory and process behind calculating the optimal geometry for flexures was of paramount importance in this work, and the same general idea was applied to every piece that would need a piezoelectric actuator. Since for an actuator to perform the expected displacement this one is required to be under the ideal load. In this work, it meant that every actuator was between a screw with a stiff surface behind and a soft structure (flexures) somewhere, but to know what force a certain bending of the material,

will exercise on the actuator, one needs to know the Euler-Bernoulli beam theory whose general equation is 3.6. Here q is a distributed force load across a beam, $\omega(x)$ gives the deflection across x, E is the Young Modulus and I is the moment of inertia of a plane area, which in this case would be the cross section of the beam.

$$q = \frac{d^2}{dx^2}\left(EI\frac{d^2\omega}{dx^2}\right) \tag{3.6}$$

However, if the product of E and I equals a constant, which would simply mean that across the beam, these properties remain constant and we are dealing with a uniform static beam, then the following expression 3.7 can be written.

$$q(x) = EI\frac{d^4\omega}{dx^4} \tag{3.7}$$

To use this expression, we should first have in mind what geometry the beam will have and where the force will be applied. In this dissertation, there were discussed three main flexures designs. The first being presented in Figure 3.9.

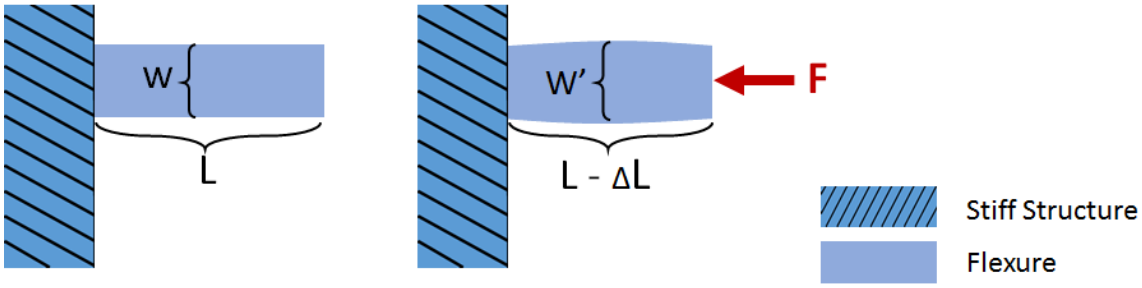

Figure 3.9: Scheme of the column flexure, before and after being under a certain force.

The behaviour of this flexure is easier to predict since given its geometry and the direction of the force applied, the relation between force and displacement is given by the definition of the Young modulus, expressed mathematically in equation 3.8. Where δL is the displacement, F the applied force, w and L represented in the Figure 3.9, are the width and length, E the Young modulus and t the thickness of the bar, not visible in the 2D perspective. This type of flexure was considered for many pieces, such as the scanner and the piece where the tuning fork holder would assemble to, but ultimately it was only used in the Z control stage to test the scanner while other pieces were still being designed or awaiting delivery. The main advantage of this flexure is that the assumptions made on the calculations to predict displacement-force relation, are identical to the geometry and conditions of the flexure in practical use, while the others are approximations.

$$\delta L = \frac{FL}{wtE} \tag{3.8}$$

However, the column flexure didn't fit with a lot of designs and so, other flexures were planned and studied. For these, it was necessary to employ the equation 3.7, which

is a differential equation that requires four assumptions to constrain it and allow for a solution to be reached. In its stead, the assumptions depend on the flexure geometry and localization of force applied, so the design of the fixed beam will be presented first, in Figure 3.10.

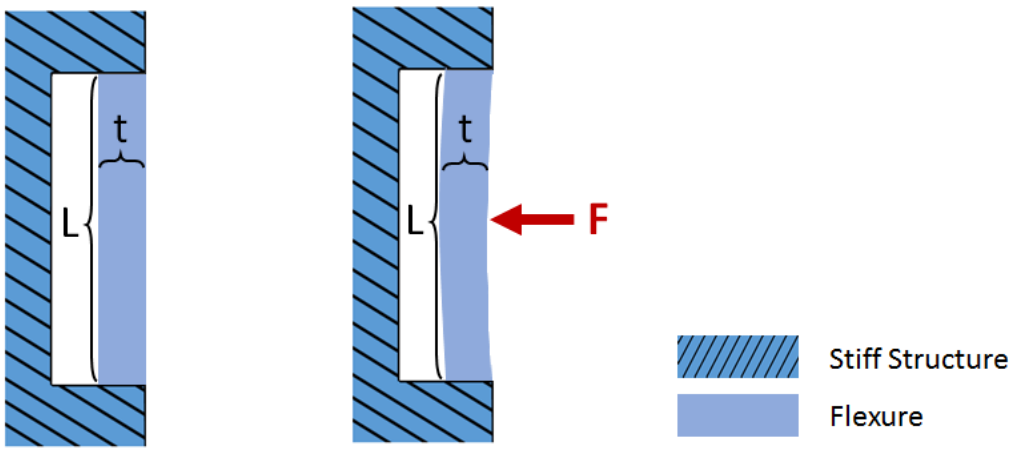

Figure 3.10: Scheme of the fixed beam flexure, before and after being under a certain force.

To solve the differential equations, we need to express the assumptions in mathematical form, so analyzing the geometry, the first assumption made was that both ends of the beam were fixed, meaning that when $x = 0$, the deflection ω will be zero as well. But not only will it have no deflection, it will also not have curvature, which means that ω derivative in $x = 0$ will also be zero. Another place where we can expect to have no curvature is in the inflection point, precisely where the force in being applied, which in this case is at half length, resulting in, ω' at $\frac{L}{2}$ being zero. The last assumption was the hardest to grasp and it stems from equation 3.7, while assuming that the force load is applied on one point only, at $\frac{L}{2}$ in the beam. After defining the assumptions the function *DSolve* was applied in the program *Wolfram Mathematica* to solve the differential equation with the following boundary conditions:

- $\omega(0) = 0$
- $\omega'(0) = 0$
- $\omega'(\frac{L}{2}) = 0$
- $\omega'''(\frac{L}{2})EI = \frac{F}{2}$

With this method the equation 3.9, describing the deflection-force behaviour of the fixed beam was reached.

$$\omega(x) = \frac{F(3Lx^2 - 4x^3)}{48EI} \tag{3.9}$$

However some pieces, like the final scanner and the piece where the tuning fork holder would be assembled, didn't mesh well with this geometry, so a last flexure was designed, which can be observed in Figure 3.11.

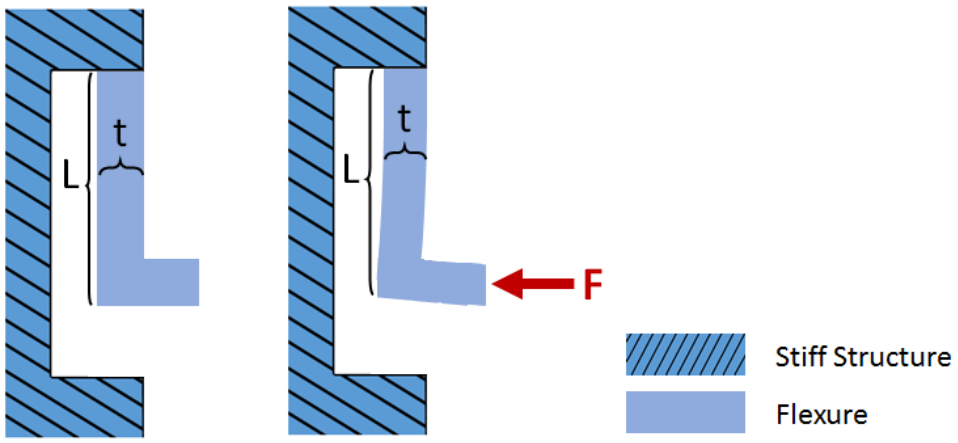

Figure 3.11: Scheme of the cantilever flexure, before and after being under a certain force.

Once again the differential equation needed four conditions to be solved, and since the cantilever flexure also has one of its sides fixed, the first two boundary conditions of the previous design remain valid. As to the third, since the "head"of the cantilever has a much larger t, it can be assumed that its curvature will be negligible, even though the deflection will be the highest of the whole bar-cantilever. So the third condition will express that, at $x = L$, ω' will be zero. Finally, the last assumption is similar to the fourth assumption of the previous flexure, but instead of applying half of the force on the halfway point of the bar, the full load force will be applied at the $x = L$, much like last time, this assumption is an approximation because the force will be distributed in a small area instead of one point. The boundary conditions used in *Wolfram Mathematica* for this flexure were the following:

- $\omega(0) = 0$
- $\omega'(0) = 0$
- $\omega'(L) = 0$
- $\omega'''(L)EI = F$

The equation attained with this method was 3.10.

$$\omega(x) = \frac{F(3Lx^2 - 2x^3)}{12EI} \tag{3.10}$$

In these equations, the dimensions of thickness and width were taken into account by the moment of inertia which is given by $\frac{t^3 w}{12}$. Since the company that prints our pieces

has the Young Modulus of the materials in display, we simply fixed some convenient dimensions and varied the others to attain a result of Xμm, given the ideal load in each respective case. This ideal force had to be divided by the number of flexures in each direction, and the calculations were made, so that the midpoint of deflection occurred for said ideal force, so that when varying the force, it will average the ideal one.

3.2.5 Applying approximately ideal load onto the piezoelectric actuators

The force load applied to the piezoelectric actuators is one of the crucial factors to take into account when trying to guarantee that the actuators will work as planned. The load will affect their resonance frequency, which needs to be much larger than the operating frequency, because if it is not, it would alter the displacement the actuators are capable of. The load will also affect the actuators maximum displacement possible, meaning that if ideal load is not secured, they might not reach the necessary displacement.

To apply the ideal load one needs to be able to measure or know the load that is being applied. Ideally, this task would be accomplished by using a sensor plaque, for example, placed between the screw head and the ceramic plate of the actuator, which would measure the force as we applied it. However, that was not possible so we used a high-resolution camera connected to the computer. Initially the camera was held by a device next to the scanner, but when tightening the screws connected to the actuators the macro stage would slightly slide. So we screwed a taller M4 screw to the scanner, and assembled a rod where the camera would be held to. This way, even if the macro stage and scanner slightly slide, the camera will move simultaneously and the image will be stable. This set up can be observed in Figure 3.12.

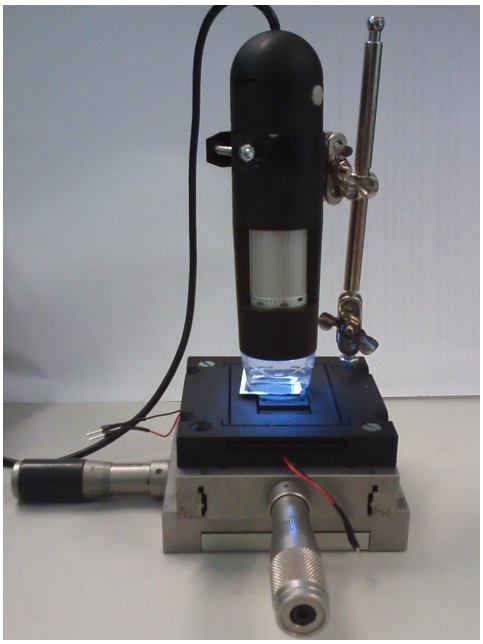

Figure 3.12: Set up used to measure load applied onto the piezoelectric actuators.

The camera allows the observation of the scanner movement during the tightening of the screws. To quantize this movement, a calibration sample whose size of the micrometric features are known, was placed on top of the scanner and used as reference. In subsection 3.2.4, the displacement generated by a certain force was calculated for the tensors of the scanner, so it was known beforehand that a displacement of approximately 250μm would be needed for and ideal load of 144N to be applied. This load of ideal operational use, was identified by the company *Thorlabs* the manufacturer of the actuators.

During the process of assembling the set up and adjusting the calibration sample, there exists a risk of contaminating the calibration sample, so we printed a calibration sample. By using *Gimp* an image manipulation software, an image was created with squares separated by 200 μm in X and Y, which was the best the printer available could reliably make, but still within the necessary requirements. We measured the distance between two squares on the computer and moved that distance plus a fourth of that distance securing the 250μm displacement without endangering the calibration sample. A photo of the printed calibration sample, taken by the camera can be seen at Figure 3.13. It is worth mentioning that this is the view of the sample before zoom, since with zoom the camera can show a 1.2mm for 1.2mm image, where only 5 to 6 squares can be seen per line, which was what we used.

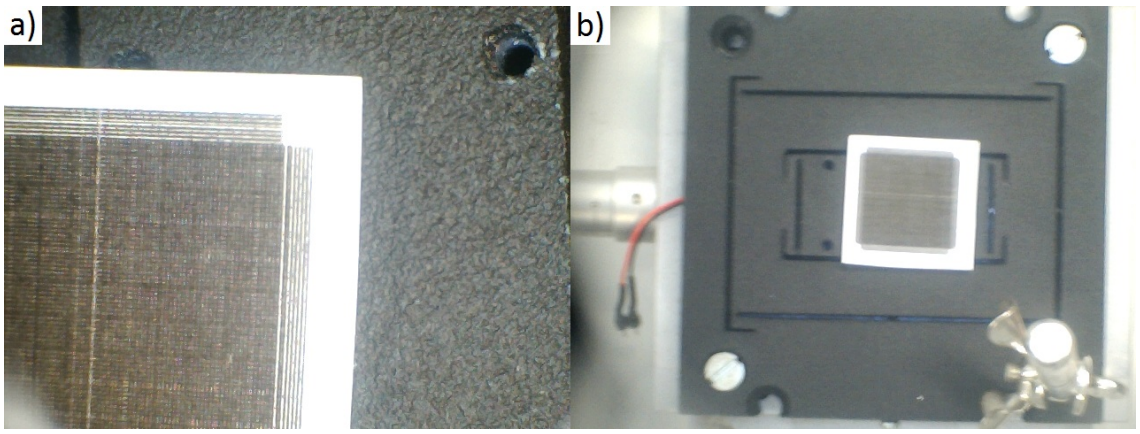

Figure 3.13: a) Closer photography of the printed calibration sample. b)Wider perspective of the printed calibration sample on the scanner.

3.3 A novel way of controlling applied loads

Several tests were performed in order to understand if the load applied onto the actuators was even, and if it resulted in equal movement by the actuators. An idea came up, to use the tuning fork as an indirect load sensor. As already presented in the theoretical review section 1.2, more specifically in expression 1.1, the bigger the excitation amplitude A_{exc}, the larger the tuning fork amplitude will be. Since we can monitor the tuning fork amplitude, we can measure if the scanner movement is bigger or lower by using the

scanner to excite the tuning fork. We stuck a tuning fork holder to the scanner with adhesive tape and introduced an excitation signal with frequency equal to the tuning fork resonance frequency, onto one of the actuators. With zero load, the actuator won't push the scanner walls and the tuning fork amplitude will be close to zero, but as load is progressively applied, the actuator will displace the scanner more and more, until it reaches its maximum displacement. From that point onward, as load force is continuously increased the actuator will be pressured and not able to displace as much, meaning the A_{exc} will be smaller, and consequently we will measure a lower tuning fork amplitude.

Figure 3.14 shows the tuning fork amplitude signal while searching for ideal load, with the method described above.

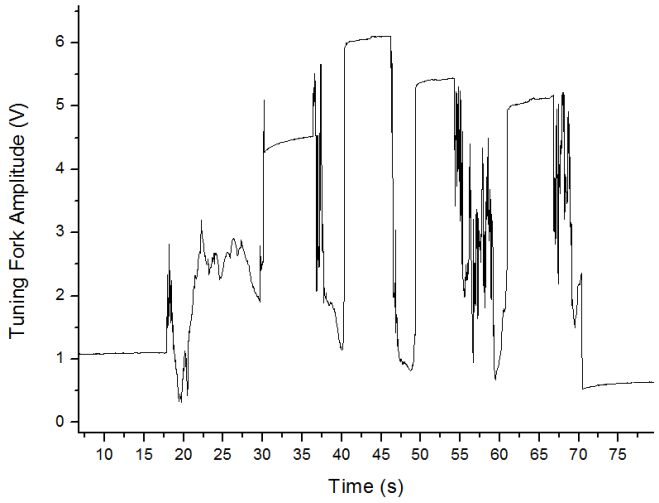

Figure 3.14: Tuning fork amplitude signal during experiment, where force load onto the actuators is being varied.

It is possible to see that between the plateaus in the graphs, where the force wasn't being varied, there appears to be hectic zones, those occur, due to coupling between the hand, screw driver and the screw, which end up acting as a damper and source noise to the system.

The method presented in this section can be used with other oscillators in any displacement setup, that requires a specific load, as long as it is capable of operating with the resonance frequency of the chosen oscillator. In conclusion, it is possible to guarantee with this technique, that the force applied will be the one that causes the most movement displacement, which is very important not only for the scanner range, but also to secure that both axis move similarly.

3.4 Design - Tip Production Setup

In contrast to the cantilevers of the laser based AFM, there isn't mass production of tuning forks with tips already glued to them. Although at first this may seem a disadvantage,

the fact that the cantilevers are expensive and fragile means that alternatives should be considered. Regarding the tuning forks as an alternative, they are cheap and the process of making and gluing tips to the tuning forks are of relative ease and economical, which is another advantage of having a quartz sensor AFM.

This stage requires the production of a sharp tip, with the ability to easily glue it to a tuning fork. For this AFM, we were aiming to make tips with 0.5 to 1 millimeter of height, presenting a conical shape where the base diameter would be 0.125 mm and the apex of the tip on the cone in itself having, less than 100 nm. In literature, there are already extensive studies on how to make sharp tips that can be used for, Field Ion Microscopy (FIM), Scanning Tunnelling Microscopy (STM), AFM and other areas, through chemical etching [39].

In this work, the *lamellae drop off technique* was employed, whose set up can be observed in Figure 3.15. This technique requires NaOH (sodium hydroxide) with a molar concentration ranging from 2M to 3M to act as an electrolyte, two rings of stainless steel, to act as electrodes, that won't deteriorate while the chemical etching takes place. The tips are obtained by using a tungsten wire, glued to the tuning fork, which in this work had a radius of 0.125 mm and applying a DC voltage that can go from 2V to 9V to the rings. Then current will flow through the wire prompting the chemical etching reaction, that is mostly described by chemical equation 3.11, to take place creating two tips.

$$W + 2H_2O + 2NaOH \rightarrow 3H_2 + Na_2WO_4 \tag{3.11}$$

The "recipe"described, including molar concentration and DC voltage values, was consulted from article [40]. The wire's own weight will pull the lower part down, helping the tip formation and impacting its shape, once the region where the etching is taking place gets thin enough, it will break apart creating two tips. This means the etching process will halt on its own, since the tungsten wire won't be connecting both rings and there will be no current flowing between the NaOH and the tungsten. This is an advantage since in other systems, like the one where only one ring is used, the user is required to cut the power supply, usually by adding an additional software program control, to guarantee that the etching on the upper part will stop, at the same time as the power part.

The first step in the process of producing a tuning fork with a tip, is gluing a very small wire to the tuning fork, which requires a lot of precision to get the right position and with the right angle to the tuning fork. Besides that, every element of the set up needs to be held at the right distance, with stable connections between the rings and the power supply. As such a set station capable of fulfilling the requirements had to be built.

3.4.1 Board production planning and design

To control the positions X and Y of the wire relative to the tuning fork, a micro metric table already available in the laboratory, capable of moving 5 millimeters on each axis, is

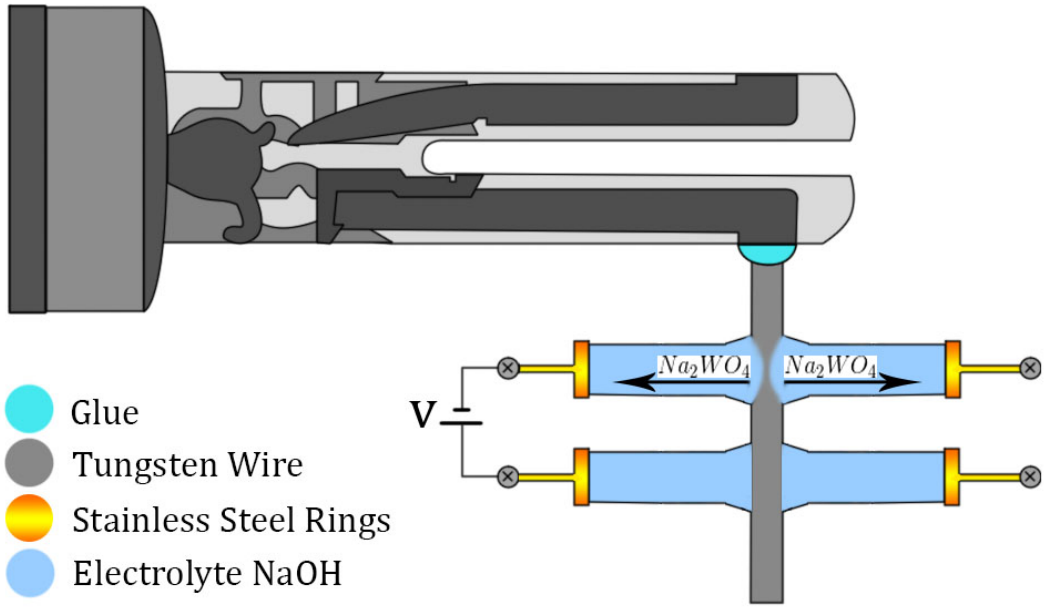

Figure 3.15: Representative scheme of the etching technique used.

used. This table with four M2 holes, can have a structure fasten on top of it. This same structure, needed to have a compartment where a 0.125 mm wire could be kept straight, and a place to allocate the rings that would have to be firmly connected to the power supply. The design of the resulting structure is represented in Figure 3.16.

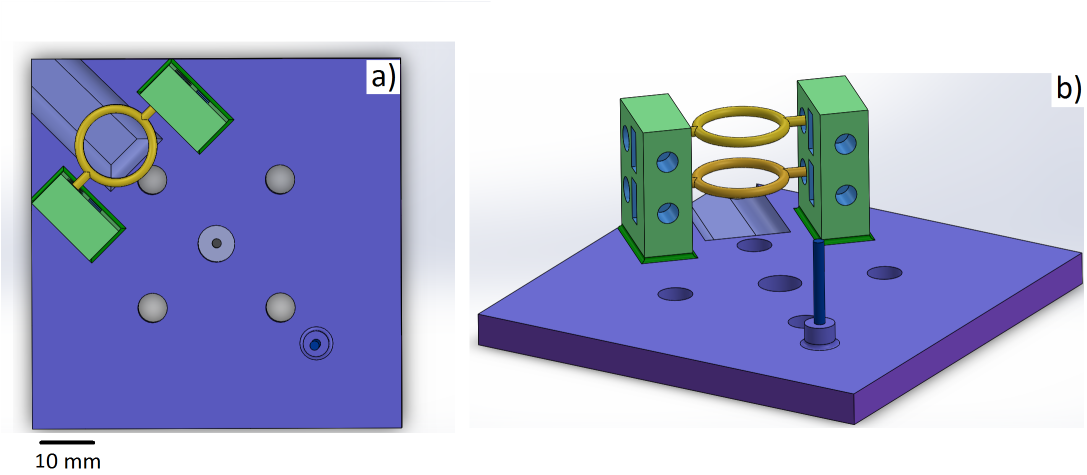

Figure 3.16: Board that holds the wire compartment and rings for the chemical etching process; a) top view and b) side view.

To hold the wire straight the needle of a normal syringe was glued to the manufactured board, that is represented in the drawing as the dark blue cylinder 3.16. This is where the wire will be placed pointing up, when the tuning fork with a very small drop of glue, stuck to a height controller system comes down to attach the wire to the tuning fork.

Then the system moves up and the wire is placed in the rings.

The board was also designed so that it could be notched to the previously mentioned the micro metric table. However, a better solution for moving the board relative to the glued wire was designed. Since the height controller is fixed, it is necessary to move the manufactured board, but rather than readjusting the X and Y axis, the board rotates 180°, thanks to a a central hole where a magnet is held. It is possible to release the board from the table readjust it and simply lower the tuning fork. Once that is done, assuming the meniscus is already formed on the rings, the energy supply is turned on and etching begins.

It is possible to see from the *side view* that the towers holding the rings, have several holes, which will allow screws to press against the extrusion on the rings. The final assembly, with the power supplying wires connected to the screws, which in place will be fixing and supplying the rings, can be better understood by viewing Figure 3.17.

It is worth noting, that the central whole for the magnet was designed in a way that prevents the formation of internal air bubbles.

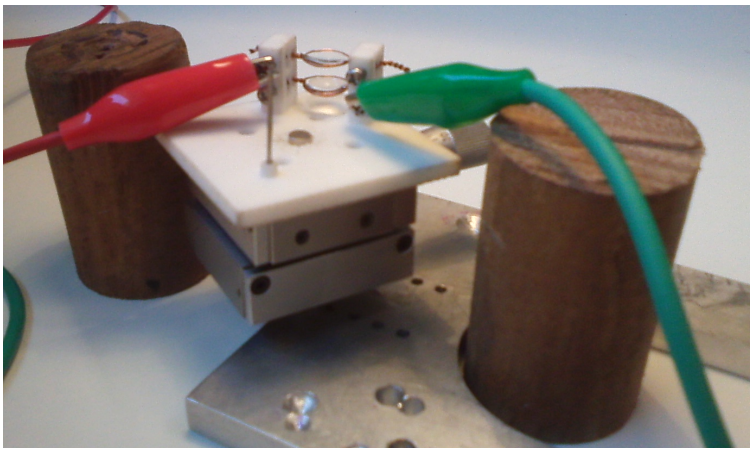

Figure 3.17: Tip setup piece assembled on the micro metric table, with meniscus formed on the rings.

This photo also includes formed meniscus on the rings, that in this picture were made out of copper and still allowed to make sharp tips with an expected radius of less than 100nm at the apex, according to the literature [39, 40]. A photo captured with a *Veho* micro camera can be found in Figure 3.18, there a long sharp tip and a short sharp tip can be seen, generally speaking the short tip is better because it is more unlikely to act as an additional coupled oscillator.

3.4.2 Height controller planning and design

The following structure served two purposes on this dissertation work. Not only would it be the permanent height controller for the tip production set up, but since the order and delivery of the pieces can take quite some time, as it took, for bureaucratic motives related to the funding entity, it was also meant to be used as a temporary Z controller

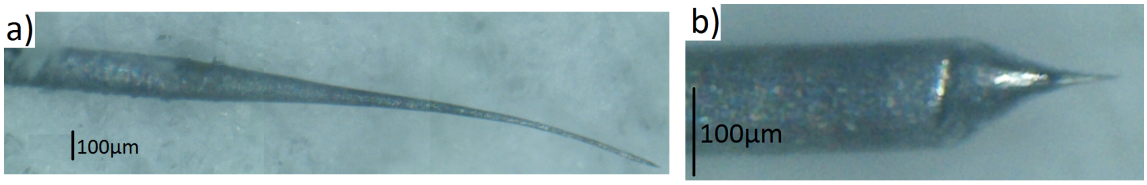

Figure 3.18: a)Photo of a long sharp tip made with the setup b)Photo of a short tip made with the same setup but a different voltage supply.

to test the scanner and perform other experiments. As such, the requirements for this structure, besides being efficient and low cost, were to incorporate a piezoelectric actuator capable of a 10 micrometer displacement. The actuator would have to be placed close to the ideal load and the overall structure should also capable of moving fractions of a millimeter in the Z height, within a 1-2cm range.

We use a piezoelectric actuator capable of a displacement of approximately 20μm already available in the laboratory, as well as a micro meter screw capable of moving 1,3cm with steps smaller then 0,02mm. With these instruments, two pieces were built, one was a cage with the purpose of holding the piezoelectric actuator under ideal load and where a tuning fork holder would be assembled. The other was a structure where the cage would be screwed to, along side the micro metric screw that would also be assembled there. The design of these pieces on *Solidworks* can be viewed mounted on the scanner and hovering alone in Figure 3.19.

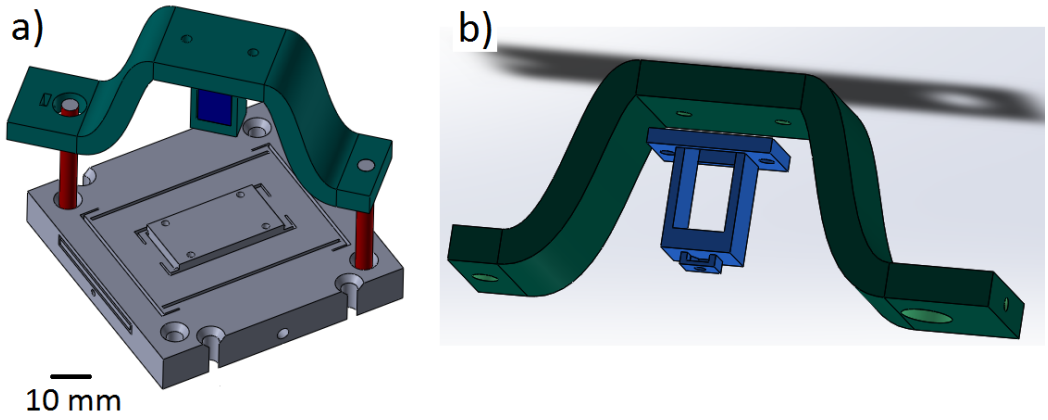

Figure 3.19: a) Height control piece mounted on the scanner, with dark blue piezoelectric actuator inside the attached cage. b) Height control piece and cage hovering separated.

Ideally this piece would have two micro-metric screws, however given it was a temporary piece, and its long term goal didn't required so much precision, a M4 screw, which is represented in red, of the Figure 3.19 part *a)*, was used. The height was controlled by locking the structure represented in sea green color between two nuts, achieving a certain approximate height with this screw, while doing the final adjustments that required more accuracy with the micro metric screw. The choice of the screws are crucial for the

purpose and functionality of this structure, namely their kind, type and length. Not only for the height control ones, but also for the one fastening the micro metric screw, which makes use of the cavity present in this one to assure stability which is key on AFM. These pieces and their assembly can be observed in Figure 3.20, alongside another piezoelectric actuator used to excite the tuning-fork mechanically, glued on top of the structure. In experiments with this stage and the scanner, the M2 screw coming out on the right side of the figure was fixed with a rubber band to the macro stage, to stabilize the height controller.

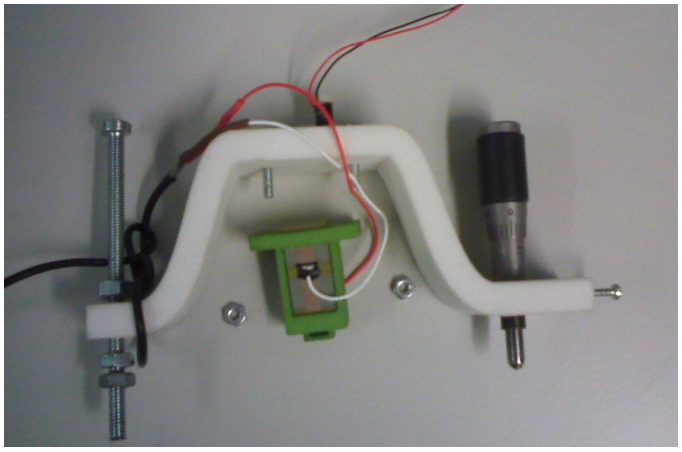

Figure 3.20: Photography of the height controller pieces partially assembled.

Lastly, this stage was completed with a cage, that had an extrusion to fix the tuning fork holder. This feature is best observed in part *b)* of Figure 3.19, where the cage is represented in blue. There can be no skidding or slipping of the tuning fork holder while topography or other operations are being made, so instead of notching the tuning fork holder to the cage, we screw it to assure higher stability. We also used the calculations and though process presented in subsection 3.2.4 to assure the cage had the appropriate geometry and dimensions, in order to apply the correct force load.

In retrospective, it was better to make the investment in acquiring another micro metric screw, since the height controller stability is crucial and there was constant use of this stage while making scanner tests and operating experiments.

To make a recap of the tip production setup here is Figure 3.21, with an inventory of the material used listed after.

Besides the material included in the figure, power supply, board production, a piece to hold the tuning fork, a hammered out spoon to place the NaOH that constituted the meniscus substance, there were also two syringes, one to move the NaOH from its recipient to the flat spoon and another to squirt some water on the materials covered in NaOH, so that these wouldn't deteriorate as fast. Another instrument that doesn't feature in the photo was a helping hand, that we started using as a very stable and articulate alternative, to manipulate the position of the tuning fork relative to the rings. Lastly, there was of course a tungsten wire, scissors to cut the wire and a tweezers to grab and

Figure 3.21: Most of the material used to produce tips.

manipulate the wire.

3.5 AFM large scale Z controller

Every AFM needs an approach system at a large scale, before trying to do a micrometric approach within the range that the actuators allow. This system is usually controlled manually by the user and then by a motor that approaches at very slow pace. To guarantee the tip won't be damaged by colliding with the sample, before the control loop can take action.

The requirements for this stage, were that the AFM should be able to move in the Z axis, a convenient distance such as fifteen to 20mm, with a step under the range of the Z control loop actuator, that was projected to have at least 10μm. Having used the temporary height controller previously, to test the scanner, we knew that the main concerns should be stability and ease of use, as such, one of the instruments regularly used to solve these requirements are micrometric screws. We took it one step further and implemented a feature that even some AFMs costing above a hundred thousand euros don't have, which is, being able to level the sample-tip slope. In other words, when the sample is tilted or the sensor is sloped in relation to the sample, the Z actuator will have to cover the slope by moving much more than the sample's actual features, while performing topography. This means that the topography will look to be displayed on a slope, which reduces resolution, and infers an overall error that has to be removed with software. It will also increase the hysteresis effect of the actuators because the actuator will have to compensate 7μm, for example, even though the features could only have a 200nm height. However, if the micrometric screws are placed in a triangular shape, any slope can be levelled by moving the screws the right distances. Nonetheless, the human user does not have the precision required to compensate slopes on the micrometric level. To solve this issue, each screw

is actuated by a motor, controlled through the computer. Furthermore, since this is a low-cost AFM, we re-utilized the built-in motors that come with CD/DVD readers, which were available in the laboratory.

With this solution in mind, we would once again need to design a piece to incorporate the motor, as well as a piece to hold the screw upside down. The piece designed to hold the motor will be presented first in Figure 3.22, and then its features will be explained.

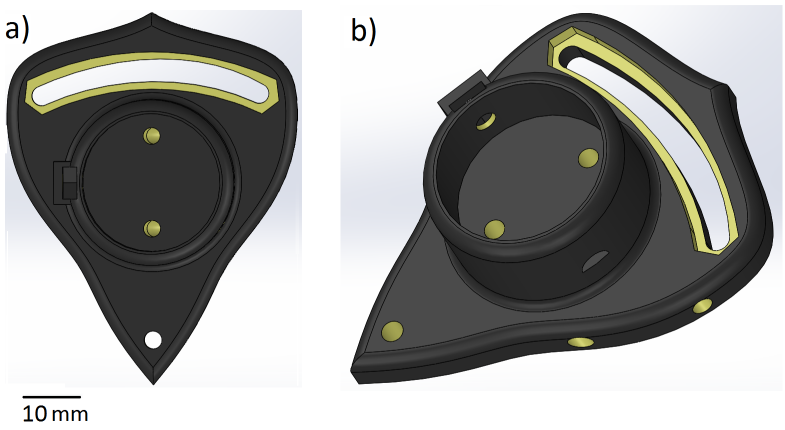

Figure 3.22: a) Top view of the motor holder piece. b) Side view of the motor holder piece.

First of all, the motor has to be well assembled on the piece, so that the elastic belt connecting it to the micrometric screw won't tilt the motor. To that end, a space for a nut where a screw goes through and fixes the motor was designed, this feature can be seen to the left of the motor cavity in *a)* of Figure 3.22. Is also possible to see two holes inside that cavity highlighted in yellow, where the power supply threads of the motor will go through. Since some motors had a different location for their supply threads, another cavities were implemented and are visible in *b)*.

Applying the right tension to the elastic belt, was important for the proper control of the screws, which is why the piece design allows to apply the needed tension by withdrawing and approaching the motor to the screw. This feature is implement at the top of the piece in *a)* also highlighted in yellow. Where a fixed screw with a nut on top, will allow to slide the piece and choose its desired position.

The design with the full setup of one of the micrometric screws, can be observed in Figure 3.23.

3.6 Z coarse approach circuit and software

The design of this system is important because without it, the probability of damaging the tip while doing a manual approach is very high.

As a starting point, the Z coarse approach should be controlled through the computer, meaning that some type of Digital to Analogue Converter (DAC) would be necessary. The electronic controller used for the AFM already had a DAC built in, so we used this one.

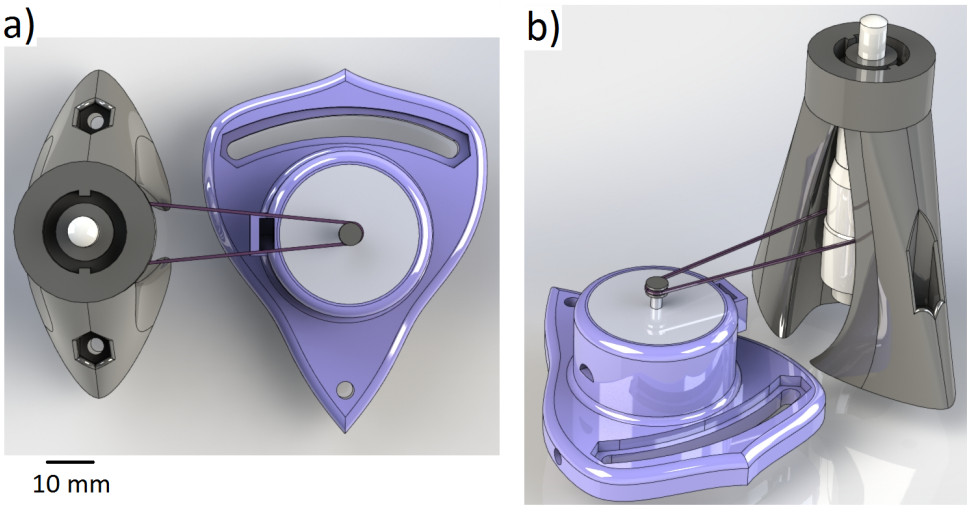

Figure 3.23: a) Top view of the setup, for one screw of the large-scale height controller. b) Side view of the same setup.

However, after determining the current and voltage necessary by the motors, to rotate the screws at a reasonable speed, it was concluded that the DAC could not output the necessary current which should be within 520 to 700mA.

To solve this issue, we used transistors, with these the DAC can use a smaller voltage to control the necessary voltage (6.5-9 volts). Still, the DAC only outputted positive voltage and is it necessary to control its signal, since the motors will have to rotate in both directions, to move the screws up and down. The presented solution in Figure 3.24, uses transistors and also allows the DAC to control the tension employed on the motors, is a known circuit called the H Bridge.

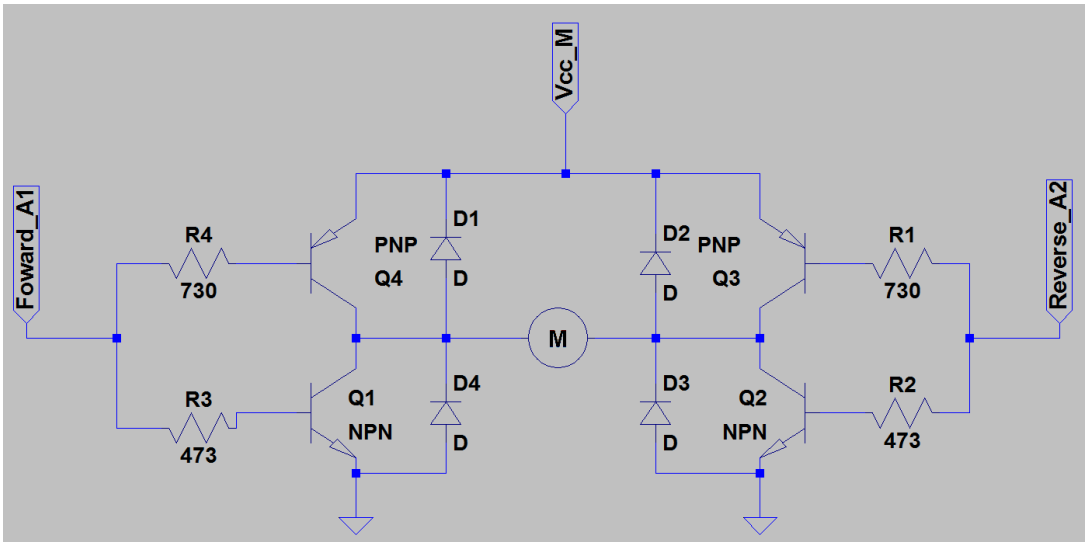

Figure 3.24: An H Bridge circuit, used to control each motor with the in-built DAC.

3.7 Z control loop and tuning fork holder

In the previous section 3.5 the design of the stage responsible from large Z movements was discussed, in this section the choices made on the stage, responsible for applying the Z loop control as well as the sensor holder will be explained.

It was necessary for this stage to move within a range of at least 10μm, so once again we used a piezoelectric actuator to generate the displacement. After choosing an actuator capable of moving 13μm we started designing a piece capable of integrating the actuator and allow for the tuning fork holder to be assembled. The final result is shown in Figure 3.25.

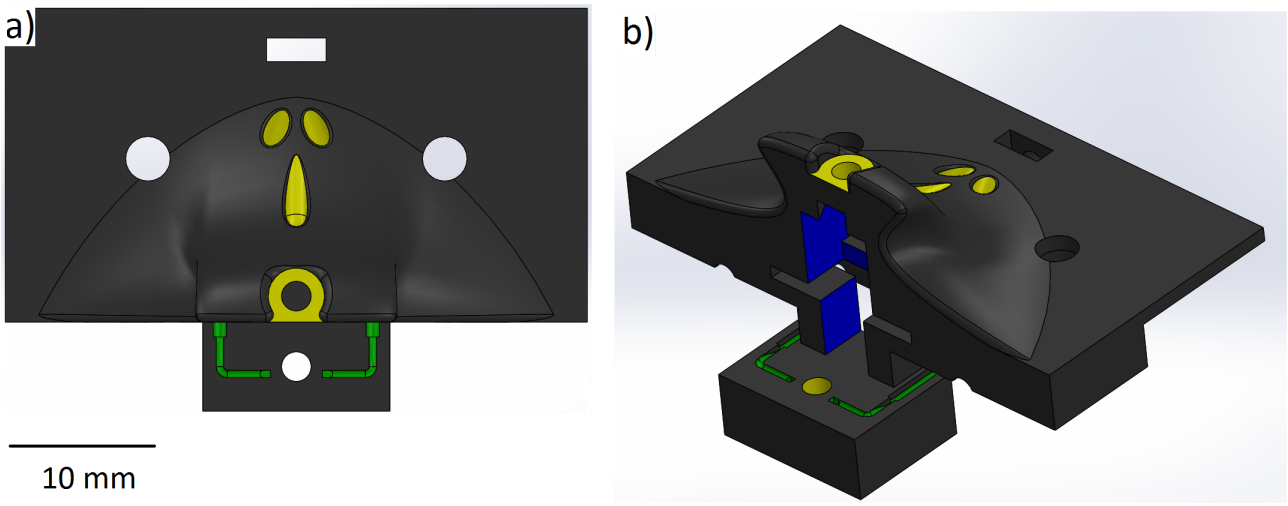

Figure 3.25: a) Top view of the Z control piece. b) Side view of the Z control piece.

There were some features added to this piece, that are related to the traditional beam deflection capability of the AFM, since this work only concerns the AFM using a tuning fork they will not be discussed. The features that are relevant to this work are highlighted in the Figure 3.25. In *b)* the feature highlighted in blue is where the actuator will be harbored which is precisely align with the screw hole of the screw that will place the actuator under a force load. This feature actually consists in two cantilever flexures, whose process behind determining their dimensions was already explained in subsection 3.2.4. Visible on *a)* are several tubes made for the actuators supply cables and tuning fork cables. Lastly there's a bolder with green features, which allows a tuning fork holder to be assembled on this piece.

The features in green were added after testing the scanner, where a lot of user inconveniences with using that setup for a tuning fork were detected, mostly from cable connection. To solve this issue, the design allows to innately connect the cables when the tuning fork holder and the Z control piece are assembled, without the necessity of manually fixing them together. To this end, the recesses highlighted in green were added.

The tuning fork holder complements this last piece, by guiding the tuning fork cables

until they reach, two recesses that will intersect the green features, once both pieces are assembled. The tuning fork holder piece is displayed in Figure 3.26.

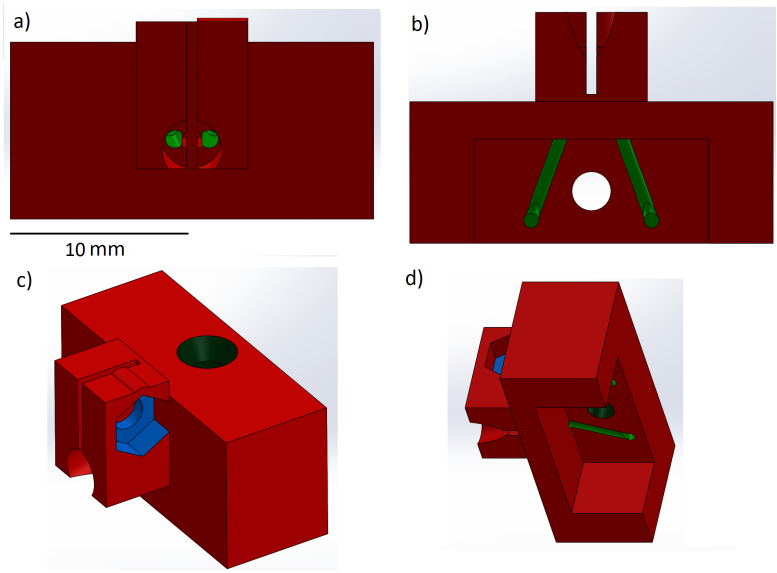

Figure 3.26: a) Front view of the tuning fork holder. b) Bottom view. c) Up side view d) Bottom side view.

Besides having been designed to assemble with the Z control piece, by screwing them together through the dark green tube in *view c*, this piece also has a couple interesting features. The aperture where tuning fork enters, has a 15° angle, so that there is always one element closer to the sample to act as a tip. It is also very important that the tuning fork is well fixed to the holder, otherwise it could slide during the AFM use and continuously change the tip-sample interaction. To guarantee this is not an issue the holder piece has a changeable hold radius. This is accomplished, by having a gap between two blocks which is more apparent in the upper part of *view b)*, as well as a nut and screw holes highlighted in blue on *view c*, that will pull the blocks together compressing the tuning fork cylindrical base inside the piece.

It is important to note that, even though this piece can be used on tuning forks with different sides, thanks to its changeable hold radius, we wanted to be able to use various sizes of tuning forks on this AFM, so another piece similar to this one, but with an even smaller hold radius was also designed. Furthermore it is also worth mentioning, that this piece was planned so that there was enough space to have a small piezoelectric actuator, responsible for mechanically exciting the tuning fork, which was already available in the laboratory. The localization of this actuator is very important, because the excitation of the tuning fork, ideally shouldn't vary with any other factors besides the actuators excitation. Meaning that it should be as close to the tuning fork as possible, which is why it was placed right above the tuning fork, where there should be no noise source couplings to the excitation.

3.8 Transimpedance amplifier

Given that the charge induced on the quartz electrodes of the tuning fork, only generates current in the nano amperes order of magnitude, the amplification of this signal without adding noise or losing data, due to low bandwidth, is of paramount importance.

The laboratory already had a transimpedance amplifier, however it was incorporate in another electronic component, and building and independent was important because as it will be explained, the lower the distance between the tuning fork and the amplifier the better, meaning the amplifier should be incorporated in the AFM body. Which raises another requirement, the circuit should be able to fit the top plate of the AFM to stay very close to the tuning fork, so it can't be very big.

The three main concerns taken into account when planning this transimpedance amplifier were, what gain will be necessary, how big does the bandwidth need to be and how to minimize noise. The circuit of the transimpedance amplifier built and used, is shown in Figure 3.27.

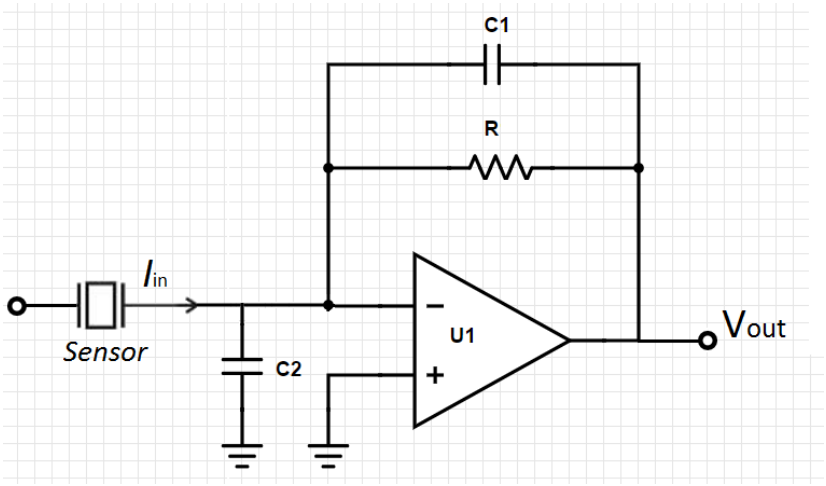

Figure 3.27: Electric circuit of a current-to-voltage converter used to amplify the signal from the tuning fork.

In this circuit the output is given by equation 3.12, where R is the resistance, I_{in} the current that comes from the tuning fork, f the frequency of the signal, C_1 the parasitic capacitance present in the resistance R and f_c the corner frequency given by $\frac{1}{2\pi RC_1}$.

$$V_{out} = -\frac{RI_{in}}{1 + i\frac{f}{f_c}} \tag{3.12}$$

From this equation, it is possible to deduce the current to voltage gain the circuit has when $f \ll f_c$, which is approximately $-R$, so as long as f_c is much larger then $30kHz$, which is approximately the frequency at which the tuning fork will be working, it is possible to determine gain, only with R magnitude. However, a gain of $10^7\Omega$ is the most advantaged one, which requires the use of a resistance with at least $10^7\Omega$, and it also means the approximation is no longer viable, so it is necessary to determine the gain equation. Since

equation 3.12, has a complex parcel, which describes the phase shift of the amplifier, we will need to know the modulus of the equation. After separating it into two parcels a real and a complex one, the gain modulus is presented in equation 3.13.

$$Gain = -R\sqrt{\frac{1}{(1+\left(\frac{f}{f_c}\right)^2}} \tag{3.13}$$

Besides the gain the circuit will also shift the phase of the signal by θ which is giving by expression 3.14.

$$\theta = arctan\left(-\frac{f}{fc}\right) \tag{3.14}$$

The parasitic capacitance of a normal resistance is well known and sometimes mentioned in the literature, for example in article [25], given as 0.2pF, which gives an f_c of approximately 80kHz.

For a frequency signal of 32kHz and a resistance of $10^7\Omega$ the gain expected for this transimpedance amplifier will be approximately 9.2×10^6, which is inside the intended range. The corner frequency with this R is at 80 kHz which is sufficiently bigger than the 30-40kHz that the tuning fork might use, meaning there is the necessary bandwidth.

With the gain and bandwidth analysed there is only the noise to take into account. The bigger the distance between the sensor and the amplifier is, the more extensive the cable connecting them will have to be, meaning that its capacitance C_2 will be bigger. This is something to take into account because C_2 is related to the noise gain, meaning that a larger cable will introduce more noise to the signal [41]. More details like this one, that come from a deep analysis of the transimpedance amplifier can be found in literature [42].

3.9 Final assembly of the AFM

In this stage the pieces were assembled, although most of them were already shown and discussed, the rest and their features will be explained from the bottom to the top of Figure 3.28.

The base plate of the AFM was designed so that the AFM could be hooked with long elastics. Since the tuning fork is very sensible to vibrations these four elastics had to be included in the design, to act as a damper to the mechanical noise. The design also allows the position of the AFM in relation to the base plate to be chosen depending on whatever is more convenient for the user and to employ a camera, or other instruments, on the AFM.

Because of the micro-metric screws height it was necessary to place a spacer bellow the scanner and the micro-metric table, so that the screws could fit under the triangular top plate. The top plate also has many cavities for the same reasons and a system to make an additional control of X and Y position was implemented. The aperture in front of the

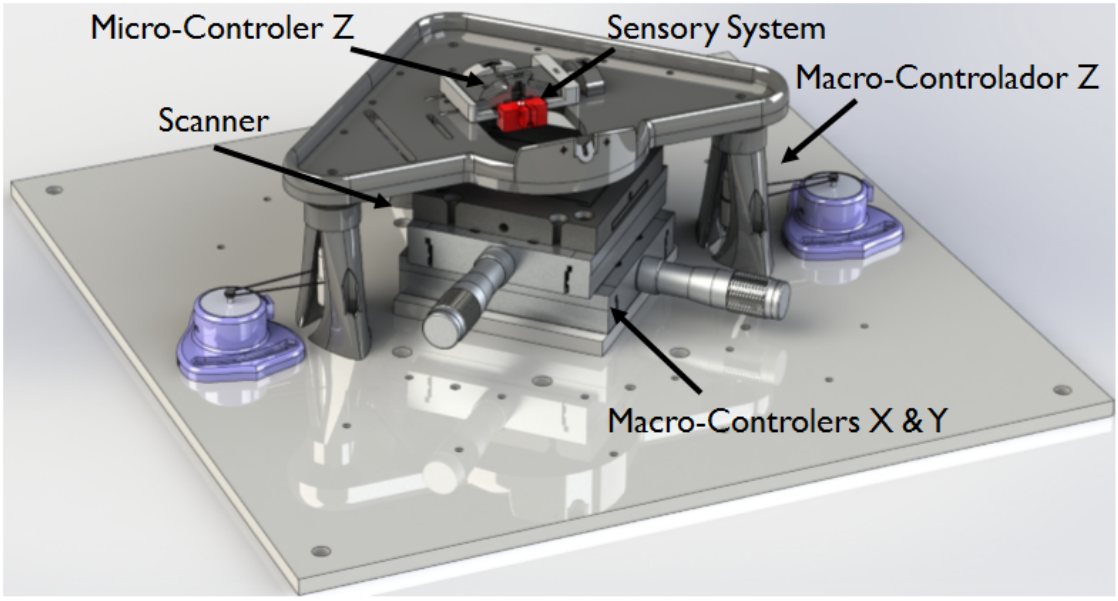

Figure 3.28: Final design of the AFM with the assembly completed.

red piece (tuning fork holder), is shaped so that not only can it have the holder and the tuning fork, but also gives a clear view of the sample if a camera is set up above, as shown in Figure 3.29.

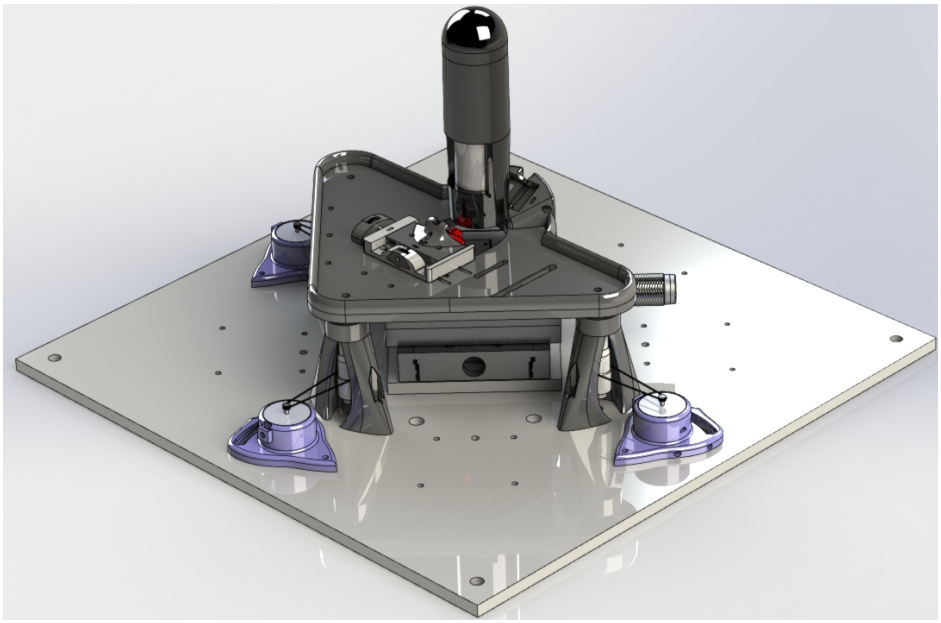

Figure 3.29: Final design of the AFM with a camera assembled.

Since an important feature of this work is that the AFM being developed has a very low cost in comparison to a commercial one, it is relevant to do a brief analysis of the costs. However the price of each component is heavily dependent in the model and company from which is bought so the analysis done here will be a rough estimate. The

most expensive part of an AFM is the electronics necessary which in this work weren't homemade, the lock-in, amplifiers and DAC, jointly can cost 6000-7000 euros, while the pieces used to build the body of the AFM, the Z macro-controler, the scanner and so on can jointly costed less than 800 euros, lastly the stage where tips are produced and the necessary materials, tungsten wire, the golden rings and so one can cost 450 euros which will give enough material to produce tips for many years. So overall the AFM costed roughly 8000 euros, which is a very low cost in comparison to the 120000 euros or more that a commercial one costs.

Chapter 4

Tuning fork and the measurement of Young Modulus

4.1 Acquiring interaction data to calculate the interaction spring constant

In its essence, the tuning fork is a damped harmonic oscillator with various vibration modes. As such, we can start by assuming its behaviour will follow the general equation of a harmonic oscillator, where K_{Res} is the spring constant, γ the damping coefficient, and x the displacement of the tuning fork prong.

$$F_{Res} = -K_{Res}x - \gamma\dot{x} \tag{4.1}$$

To work with the tuning fork it's usually necessary to excite it to the resonance frequency. This means the resultant force F_{Res} will depend on another excitation force represented by $Kx_0cos(\omega t)$, making the resultant equation 4.2. This is the equation of a damped forced oscillator, when the applied frequency is equal to its natural frequency.

$$F_{Res} = -K_{Res}x - \gamma\dot{x} + Kx_0cos(\omega t - \phi) \tag{4.2}$$

However, equation 4.2 doesn't represent the movement of the tuning fork, when interacting with the sample. For this reason the spring constant associated with the interaction K_i, and the damping caused by the interaction γ_i, onto the oscillator movement has to be taken into account. After making these adjustments to the equation 4.2, becomes:

$$F_{Res} = -(K + K_i)x - (\gamma + \gamma_i)\dot{x} + Kx_0cos(\omega t - \phi) \tag{4.3}$$

As it will be observed further in the work, it will be very useful to have expressions that describe the spring constant and the damping coefficient tip-sample interaction, in

other words, K_i and γ_i. By replacing x, the position of the tip, for $Acos(\omega t)$, and replacing F_{Res} by $m\ddot{x}$ while using trigonometric functions to simplify the equation 4.3, K_i and γ_i were determined,

$$K_i = \frac{Kx_0 cos(\phi)}{A} + \frac{K\omega^2}{\omega_0^2} - K \tag{4.4}$$

$$\gamma_i = \frac{Kx_0 sin(\phi)}{A\omega} - \frac{K}{Q\omega_0} \tag{4.5}$$

The set up to make this observation will be described. As it can be seen in Figure 4.1, the previously presented Z height controller, has another structure screwed to it, to hold and act as a flexure for the piezoelectric actuator, that will do the Z control on the micro-scale. This ensemble allows to approach the tuning fork which is set in the sensor holder, to the scanner underneath, where the Z height controller if screwed through. Lastly this set up had a macro-stage XY which was the metallic structure with 2 micrometers, placed upon a black and large sponge, which heavily damped the mechanical vibrations that could possibly come from the table.

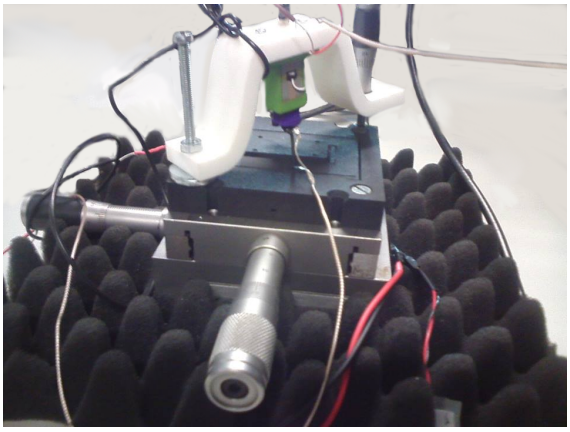

Figure 4.1: The temporary set up used to observe the tuning forks resonance curve.

In this set up, it was decided that the tuning fork should be excited mechanically by a piezoelectric actuator, that can be observed in Figure 4.1, glued on top of the Z controller piece, above the other larger piezoelectric actuator. The scanner operation and the electronics required has already been described, so we will focus on the other electronics used in this set up. The piezoelectric actuators have to be protected so the source voltage doesn't depolarize them, in this work this was done in the *Daisy* software, that controlled the voltage in the actuators, by choosing the option unipolar. It is also important that this software is correctly calibrated taking into account the maximum voltage that should be used in the piezoelectric actuators. The particular lock-in used could simultaneously act as an amplifier, a necessary component to operate the tuning fork output signal in the order of the nano-ampere.

By gluing a tip to the prong there will be a shift in the resonance frequency of the tuning fork, so when searching for the resonance peak we can assume it will have lowered.

In Figure 4.2 there is a typical result presented acquired by the lock-in, showing the amplitude and phase behavior around the resonance frequency.

Two outputs signals, amplitude and phase were connected to an *auttocube ASC 500*, that was then connected to a computer where a software displayed and recorded the data. This electronic component not only acts as a data acquisition plate, but also controls the actuator that secures the Z loop.

The phase range is within 360°, but the lock-in presents the phase with a certain offset. To convert the phase data from volts to radian it is necessary to discover the value of the offset. For that, we will use the theoretical knowledge, that at the maximum amplitude of the resonance curve, where the frequency equals the resonance frequency, the phase will be -90°. So by overlapping the phase and amplitude data as seen in Figure 4.2, it is easy to get the phase value in volts that corresponds to -90°.

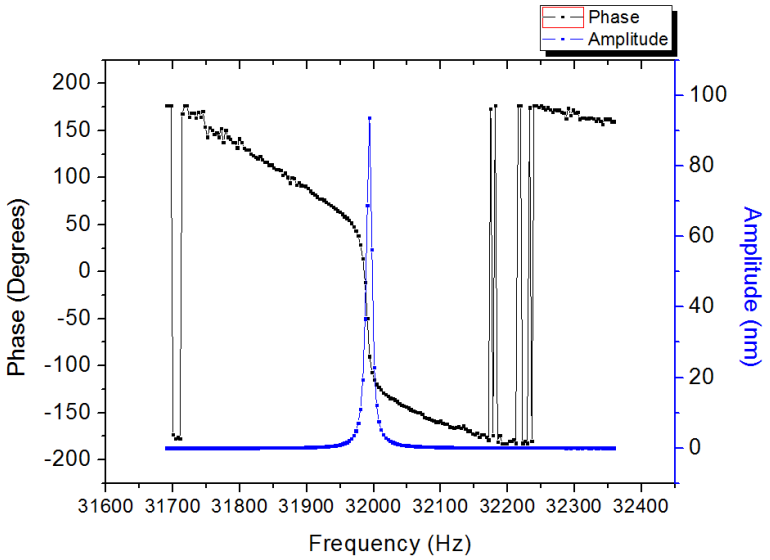

Figure 4.2: Resonance curve of a tuning fork with glue on it.

The lock-in allows the control of the sensitivity of the signal analyzes,meaning the conversion from volts to amperes is direct, as well as the from amperes to nanometers, because each nanometer movement will generate in the electrodes a two nanoampere signal.

When the data is in S.I units equation 4.4 can be applied. However for the specific case where the tuning fork is being excited at resonance frequency $\omega = \omega_0$, equation 4.4 can still be simplified, with its second parcel equaling zero, the expression becomes 4.6.

$$K_i = \frac{K x_0 cos(\phi)}{A} \tag{4.6}$$

Since the data acquired already presents the phase and amplitude, the only variables missing to calculate K_i are K, the spring constant that we knew beforehand, as 42000 N/m and x_0. Then we can use equation 4.2, that already accounts for the excitation signal,

but not for the effects of the sample-tip interaction to reach the equation 1.1, presented in section 1.2.

Since it is known the maximum amplitude occurs at resonance frequency, at which ω equals ω_0 we reach the expression 4.7.

$$A_{max} = \frac{x_0 K}{\gamma \omega_0} \tag{4.7}$$

Because $Q = \frac{K}{\gamma \omega_0}$, we now know how to calculate x_0 as long the value of Q is known. The quality constant is another value that can be extrapolated from the resonance curve, either by doing a Lorentz fit, or by taking the coefficient between the resonance frequency and the Full Width at Half Maximum (FWHM), of the amplitude resonance curve.

4.2 Contact mechanics and the calculation of the Young Modulus

To understand how K_i can be used to learn the Young's Modulus, one first needs to understand the contact mechanics expressions and what interactions they represent.

If a stiff object approaches an elastic object and is placed under a certain load, the elastic one will suffer an indentation. This indentation can occur even if both objects are elastic or stiff, in fact, the indentation is dependent on many factors, such as the stiffness of the solid materials, or in other words, the Young Modulus of each object. Another factor to take into account, is the value of the load force applied, naturally if a bigger load is applied there should be a deeper indentation. Furthermore, the area of contact will also be important, since for the same force, the pressure will vary according to the area of contact.

The first and probably most simplistic solution for this problem was presented in 1896 by Heinrich Hertz, where he described the relation between the force applied and the indentation as seen in equation 4.8. Where R the radius of an elastic sphere which will indent a half-space and E^* is a variable dependent on the Young's modulus of each material and their respective Poisson coefficients, as it can be observed in expression 4.9. The Poisson ratio of a material ν, defines the relation between a transverse strain and a longitudinal strain when a load force is being applied in the longitudinal direction, in this definition the transverse direction is normal to the longitudinal direction. Lastly δ corresponds to the indentation.

$$F = \frac{4}{3} E^* \sqrt{R} \delta^{\frac{3}{2}} \tag{4.8}$$

$$E^* = \left(\frac{1 - \nu_1^2}{E_1} + \frac{1 - \nu_2^2}{E_2} \right)^{-1} \tag{4.9}$$

The Hertz model as presented, does not account for adhesion forces, which are more relevant at the nano scale, meaning that, to calculate the elastic modulus of a material with

adhesion it is necessary to employ one of the subsequent models, like the Johnson-Kendall-Roberts (JKR) model or the Derjaguin-Muller-Toporov (DMT) model, which are models for elastic contact. There are of course other assumptions, made by the Hertz model, that have to be met to accurately calculate the Young's modulus with this model [43].

- There must be no friction between the two bodies.
- The areas of the bodies that are in contact have to be continuous and non-conforming. Meaning that the surfaces in contact are not rough and that one or two of the bodies will deform when they enter contact.
- The strains provoked on contact, by the load force must be much smaller in comparison to the contacted bodies.
- Both bodies can be considered elastic half-spaces. Meaning that the radius of curvature of the bodies are much larger than the radius of the circle area formed on contact.

This is where using a tuning fork and being able to calculate the force gradient instead of the force itself becomes an useful advantage. By accounting the adhesion force F_{ad}, while assuming the other Hertz model conditions, the force is given by equation 4.10. It is important to note that the Hertz model does not assume an additional adhesive force as presented in this expression,

$$F = -F_{ad} + \frac{4}{3}E^*\sqrt{R}\delta^{\frac{3}{2}} \tag{4.10}$$

Furthermore, assuming that there is no deformation of the tuning fork's prong while in contact and that F_{ad} is constant while varying δ, the equation 4.11 can be assumed. This means that the only unknown variables to determine the elastic modulus are $\frac{K_i}{\sqrt{\delta}}$, but of course those variables can be observed. In some cases, such as linear adhesive forces the $\frac{K_i}{\sqrt{\delta}}$ is the line coefficient of the processed experimental data, which can be found by doing a linear regression of the results.

$$E^* = \frac{Kx_0 cos(\phi))}{2A\sqrt{R\delta}} + \frac{m\omega^2 - K}{2\sqrt{R\delta}} \tag{4.11}$$

Another advantage of using a tuning fork is the lack of jump-to-contact, from the tip to the sample, that is regularly observed in force-curves made with AFMs that don't use a stiff quartz crytal sensor. The stiffness of the tuning fork is high enough that, the sensor will hold the attractive forces allowing the observation of a continuous curve. But there are also cantilevers with tips that have higher spring constants similar to the quartz crystal spring constants. The reason that the tuning fork still holds and advantage over these cantilevers is that the tuning fork has two prongs similar to each other, allowing it to have a high Q factor. By having a low Q factor the cantilever will have a broad resonance peak, meaning there will be a wide range of frequencies at which the system seems to

resonate to. On the other hand, the quartz crystals with large Q factors, act the opposite way, which means they will have a smaller error while measuring the oscillation state.

4.3 Accounting for adhesion with JKR and DMT model

The importance of being able to study nano-mechanical properties of materials was already expanded upon, but the use of a tuning fork in the AFM scientific community is mainly for AFMs with vacuum and low temperature systems, where a less complicated sensor system has to be employed. However, as shown in this work, the tuning fork's advantages can be applied in non-vacuum systems and in the study of the nano-mechanical properties. For that reason, one of the materials that we decided to study was the Poly-Di-Methyl-Siloxane (PDMS).

PDMS has a variety of uses as a bio-compatible substrate for cells [44, 45], to fabricate microsystems [46], and even other uses such as microelectro mechanical systems [46, 47]. Given its wide use and applications the PDMS mechanical properties were already extensively studied, making it a good sample to confirm that the measurements and reasoning behind using the tuning fork for these studies are correct. As explained before, the Hertz contact model does not account for the existence of adhesive forces, and studies were made on rubber to confirm that the Hertz contact model could not be applied, so a new model named Johnson-Kendall-Roberts (JKR), was proposed [48] and later a complementary model that also considered adhesive forces called Derjaguin-Muller-Toporov (DMT) was proposed [49].

The JKR model originates from the Hertz model but is then modified to take into account the stored elastic energy, which corresponds to the work that has to be done to deform the materials in contact, and the surface energy lost. Which is the energy required to create the new deformed surface. So, using the Hertz equation, when the bodies are spheres and taking these two concepts into account, the JKR model presents the following expression 4.12. Apart from γ that instead of the damping coefficient represents the adhesion, all the other variables have the same meaning already announced previously.

$$(\delta R)^{\frac{3}{2}} = \frac{3R}{4E^*}\left(F + 6\gamma\pi R + \sqrt{12\gamma\pi RF + (6\gamma\pi R)^2}\right) \tag{4.12}$$

Since what is measured with the tuning fork is the force gradient, and not the force itself, this equation needs to be iterated to give F. By rearranging the expression to give F two possible solutions emerge, which are presented in one equation 4.13. The difference between the two expressions being the signal of the second main parcel.

$$F = \frac{4}{3}\left(\pm 3\sqrt{\pi R\gamma E^*\delta}(R\delta)^{\frac{1}{4}} + E^*\delta\sqrt{R\delta}\right) \tag{4.13}$$

Since there can only be one resulting force of the interaction, one of the expressions shouldn't have physical meaning. To identify what expression has the right physical meaning, both were plotted with realistic values for R, E, γ and with δ going from zero to

0.5 nanometer. The reason to use the JKR model was to account for the adhesion found in rubber, this means that when the indentation is close to zero there will be adhesive forces between the sensor and the polymer, and these are attractive, so they are represented by the negative signal.

As stated before, the tuning fork measures the force gradient, which means the equation must be derived in function of the indentation. The final result is shown in equation 4.14.

$$F'(\delta) = -\frac{3(R\delta)^{\frac{1}{4}}\sqrt{\pi R E^* \gamma}}{\sqrt{\delta}} + 2E^*\sqrt{R\delta} \tag{4.14}$$

After plotting this function, that has a similar behaviour to that of two square root functions added, it was clear that it is viable to acquire three parameters while fitting the data. This means that if the data acquired has a very low level of noise, it will be possible to make a fit of the data and use the equation 4.14 not only to find the Young's modulus, but also to learn the sample's adhesion. This means that with one experiment, it is possible not only to study the nano mechanical properties of a material, while taking into account adhesive forces, but also find out the tips radius which is often unknown. This would mean that to know a more accurate radius, most of the times, it would be necessary to use additional equipment, like an electronic microscope.

Besides studying the JKR model, the same approach was given to the DMT model since they are complementary models and possibly necessary to determine the Young's modulus of the PDMS. The DMT model assumes that the considerations to the stress distribution and deformation fields of the Hertz model are correct, however it accounts for an additional adhesive force that results from the adhesive interaction stresses [50]. If we consider that the indentation is done by an spherical body then according to the DMT model the force is given by expression 4.15.

$$F = -\frac{4}{3}\left(3\gamma\pi R - \delta^{\frac{3}{2}}\sqrt{R}E^*\right) \tag{4.15}$$

Once again since the experimental measurements only allow us to know the force gradient, the expression that correlates the force gradient with the Young's modulus, was determined 4.1, but since according to the last expression, the adhesive force is constant despite the level of indentation, once we calculate the derivative of the DMT model we reach the Hertz force gradient expression.

All the above expressions in this section, are given when considering that the tip doing the indentation is a sphere, this doesn't mean that the whole tip is a sphere, but that in comparison to the indentation depth and contact area, the part of the tip that is in contact with the sample is similar to a sphere. Meaning that depending on tip radius and indentation level, even a chemically etched tip can either look like a sphere or a cone. For example, if the radius of the tip is 100nm, but the indentation is 4 micrometers, to the sample it would appear that a cone is indenting. To account for this in the study, some

Table 4.1: The expressions of JKR, DMT and Hertz when accounting for a conic shaped tip.

	Sneddon Model	JKR Model	DMT Model
Force	$\frac{2}{\pi}\frac{E}{1-\nu^2}\delta^2\tan\theta$	$\frac{8\delta^{\frac{3}{2}}\sqrt{2\gamma E^*}\sin\theta^{\frac{3}{2}}}{-\pi\cos\theta^{\frac{3}{2}}}+\frac{32\delta^3E^*\tan\theta^3}{3\pi^3R}$	$\frac{4\left(3\gamma\pi^4R^2+8\delta^3E^*\tan\theta^{\frac{3}{2}}\right)}{-3\pi R}$
Force Gradient	$\frac{4}{\pi}\frac{E}{1-\nu^2}\delta\tan\theta$	$\frac{12\sqrt{2\delta\gamma E^*}\sin\theta^{\frac{3}{2}}}{-\pi\cos\theta^{\frac{3}{2}}}+\frac{32\delta^2E^*\tan\theta^3}{\pi^3R}$	$\frac{32\delta^2E^*\tan\theta^3}{\pi^3R}$

further calculations were made assuming that the radius of the contact area was given by expression 4.16, which represents the contact between a rigid conical tip and an elastic half-space [51].

$$a=\frac{2}{\pi}d\tan\theta \tag{4.16}$$

By replacing the area of contact with this expression in JKR and DMT models, new expressions were attained. To ease their observation the new expressions were compiled in a table 4.1, where we are under the assumption that the indentation tip has a conic shape.

Chapter 5

Experimental Results and Tests

5.1 Scanner and AFM topography tests

A temporary Z control stage was used, before the delivery of other components, so that the scanner could be tested. It is also important to note that to make any test it is necessary to assure there wont be sliding friction between the sample and the scanner. To achieve this a sample holder already available in the laboratory was fixated to the scanner and the samples were glued with a small drop of glue to the sample holder. In case of the CD samples this was done through the use of adhesive tape which was also utilized to extract the CD data layer from the CD surface.

As a test sample, we used a calibration sample, with topography well described by the company that produces the samples. The sample used, was composed by a grid that had a series of double lines, where both lines had squares with gaps separating them, but the second line didn't align with the first one. The following Figure 5.1, presents the result achieved.

Since the Z control wasn't calibrated and is not the test subject, a Z scale was not attributed to the image. By analyzing this image, it is possible to make some conclusions about the scanner. First of all, both axis are moving and they are doing so with close to similar displacement, that is demonstrated by the shape of the squared features. For example, if the result had a clear rectangular shape, it would be possible to infer that one axis would be employing a bigger displacement than the other. On the other hand, if we could only see one line of squares, or rectangles and gaps than it would be possible that only one of the axis was moving and that the same topographic line was being repeatedly recorded. The only aspect, relative to the scanner, that needed improvement was the actual displacement of the actuators. Although we tried to utilize the actuators with their maximum displacement of 30μm, which is why the figure presents 30μm on each axis,

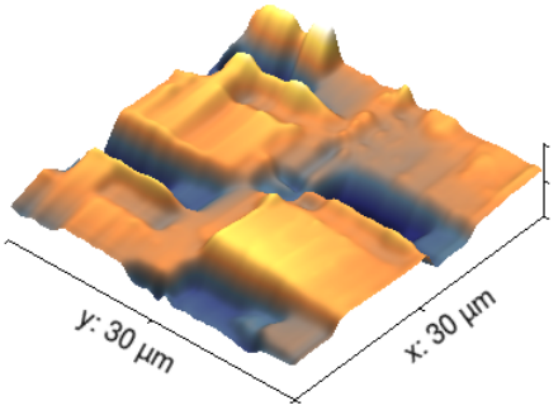

Figure 5.1: Topography of a calibration sample, made with the goal of testing the scanner.

the actual displacement was approximately 23μm on the X axis and 21μm on the Y axis. These values can be inferred because we knew the actual size of the squares from the data provided by the manufacturer.

After studying the calibration sample, we decided to use a CD to test the scanner. The CD is a good sample, because not only are the features smaller than those of the calibration sample used, but also they have dimensions known just as well, meaning we could compare the results to reliable data. Repeating the preparations and methods used to test the previous sample, the topography presented on Figure 5.2, was attained.

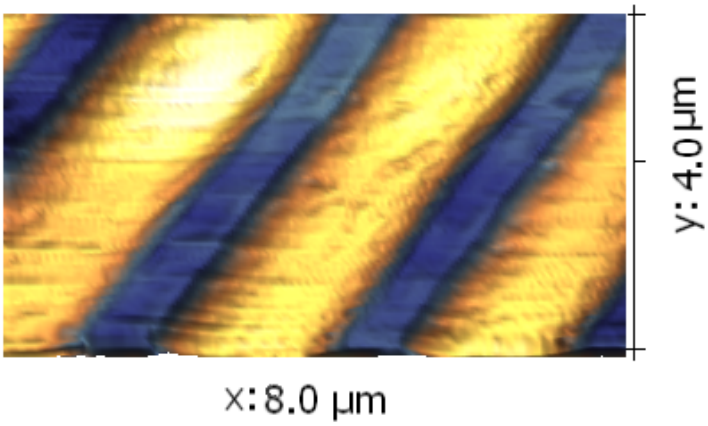

Figure 5.2: Topography of a CD, made with the goal of testing the scanner.

It is very easy to differentiate the lines from the cavities, however the real size of the CD image we observed had about double the dimensions expected, meaning the operation of the scanner was still not ideal. This could be due to, calibration of scanner was not being correct, problems with the scanner geometry or that the actuators were not properly loaded.

Using a sharp tip produced with the method described in section 3.4 and applying ideal load with method described in 3.3, we re-calibrated the temporary Z control stage as well, so that we could properly analyze the features in Z. With this set up the topography

of Figure 5.3 was achieved.

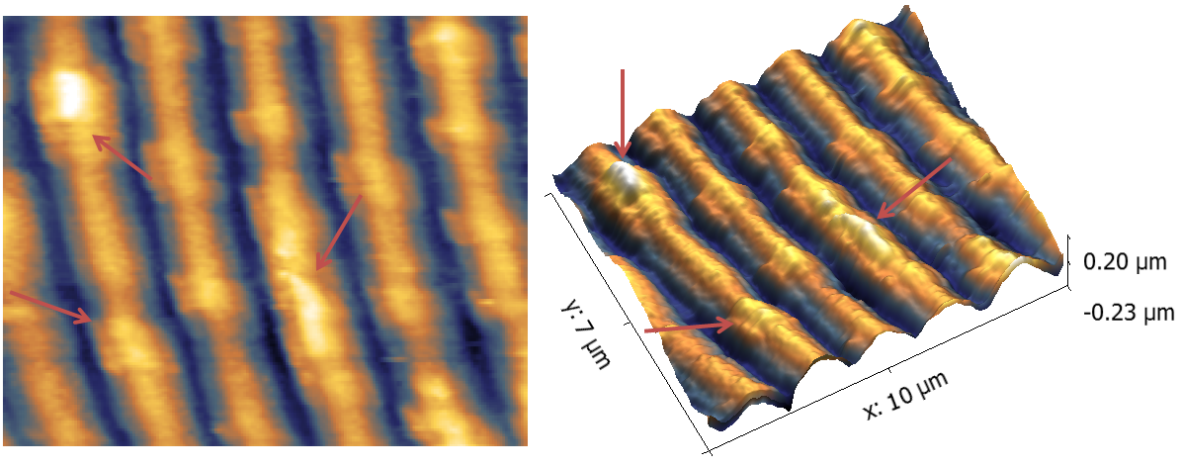

Figure 5.3: Topography of a CD, made with a better set up to test the scanner.

In this image, it is possible to observe bits presenting the expected height of approximately 50nm, as well, parallel tracks, so the scanner test is successful, however the overall quality of the image is still insufficient, which can be attributed to the temporary Z stage not being appropriate.

In respect to the AFM tests, having the scanner tests completed it is only necessary to test and improve the Z elements of topography. In comparison to the last figure presented, we should expect to find the distance between the CD tracks, of equal width to the tracks, meaning the sensors tips are sharp enough. The topography should also present a higher number of bits and more distinguishable.

The Figure 5.4, presents a topographic image acquired with the final Z stage, although it shows more distinguishable bits, the correct distance between tracks, and properly shaped tracks. In addition to the previous tests it is possible to conclude that the AFM is working, even though it still lacks in resolution when comparing it to a commercial AFM costing more than one hundred euros, which is being limited by noise sources which will be discussed further in the work. It is also worth mentioning that these images took around 20 to 25 minutes to make in average.

In conclusion, further studies should be made to identify the limiting factors, so that the required adjustments and upgrades can be made, while keeping the overall cost of the AFM very low. Some of the limiting factors were identified during use, for example, a crucial factor in reducing noise, was shielding the input cable with a Faraday's cage, which was made out of aluminium foil tightly rolled around the cable and connected to the ground. To improve the AFM in further development it should be placed inside a box, that would shield the entire AFM from electromagnetic noise. This container would also serve other purposes such as acting like an acoustic damper and it would also allow to strap the AFM base plaque to four elastics leaving it hanging and thus reducing mechanical vibrations noise. This kind of setup is commonly used in AFMs and

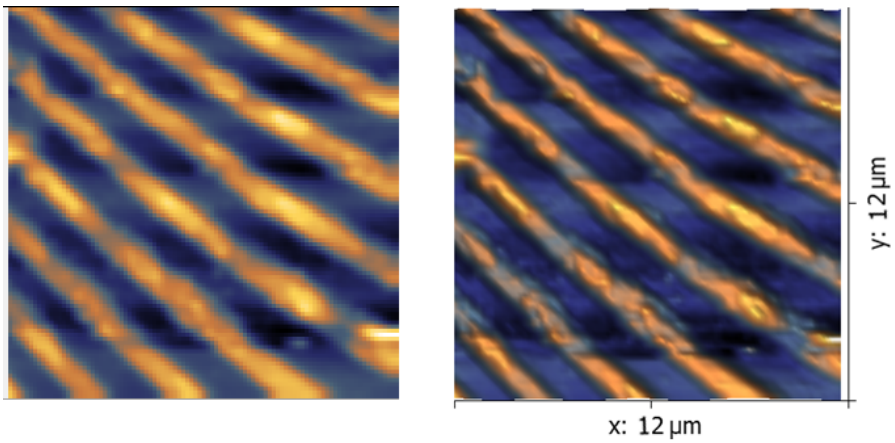

Figure 5.4: Topography of a CD, made with the first iteration of the low-cost AFM.

it greatly reduces three different noise sources, for that reason it should be the next step in improving the low-cost AFM.

5.2 Indentation tests

As mentioned before the PDMS was one of the materials studied, this a fairly well known material so it is possible to compare results. However, the mechanical properties of PDMS vary according to its curing and operational temperatures, so many studies were made to determine the influence of heating temperature on the Young's modulus of PDMS [47, 52], with more recent ones reporting a range of values between 1.32-2.97MPa depending on curing temperature [53]. Within this range the most commonly produced PDMS has a reported value of 1.8MPa [47, 54–56], so we have a good value for comparison purposes.

The method used to acquire the experimental data was already explained before, where the amplitude and phase of the tuning fork with a tungsten tip, while approaching and indenting the PDMS was recorded. After executing the experiment, the data was converted and used to calculate the constant spring K during the indentation, with the expression 4.4, so that a model could be used to fit the experimental data. Given the PDMS adhesive nature it is expected that either the JKR or the DMT model should be used and after applying both, while assuming the tip indenting was a sphere. After trying to fit the data with both models the DMT model was clearly the most suitable one to use. A fitting of the data with this model can be seen in Figure 5.5.

To achieve this fit the result of the E^* was approximately 3.61MPa, so to calculate the Young's modulus of PDMS expression 4.9 was used. This requires the knowledge of the Young's modulus of the indenter material and both materials Poisson ratio, which is known in the literature as approximately 0.5 [56]. Since the material of the tip is tungsten whose elastic modulus is also known in the literature as approximately 411GPa, the parcel of E^* relative to the tungsten can be negligible meaning all the variables needed

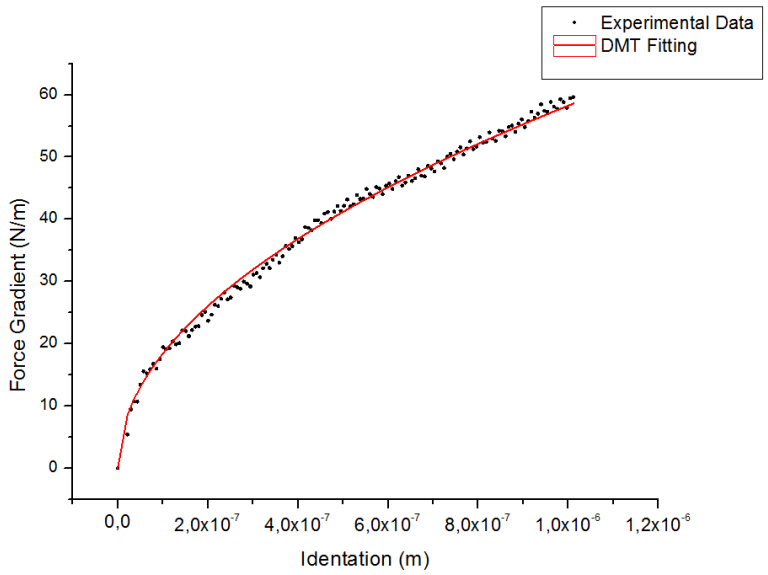

Figure 5.5: Fitting of the interaction data with the DMT model.

to calculate the PDMS Young's modulus are known, giving a result of 2.7MPa. Despite this value being inside the range mentioned earlier, we expected a value closer to 1.8MPa, however the sample of PDMS being used was not new, and there are studies into the effect of aging and storage conditions on polymers Young's modulus, where a correlation was found. The article [57] observed that as a certain polymer aged inside an air medium, its Young's modulus increased as well, so it is expected that the PDMS Young's modulus increased over time and is indeed, no longer 1.8MPa.

To determine the Young's modulus that performs the fitting with the less possible quadratic error, two programs were used, the fitting function of *Wolfram Mathematica*, and a custom-made program in *Netlogo* that uses a genetic algorithm, which will be briefly explained in section 5.4, the source code and interface for the program are also presented in the annex portion of the work.

5.3 Friction experiment using AFM and tuning fork

The capacity of acting both as a sensor and an actuator makes the tuning fork a versatile tool. As it was already shown in section 3.3 where a novel way of applying ideal load onto the scanners actuators was reported. In this chapter, another creative way of using the tuning fork in the AFM will be described.

In this experiment, the tuning fork was glued on an improvised sample holder and this sample holder was fixed to the scanner, while a cantilever was placed on the Z axis of the AFM and aligned with one of the tuning fork's prongs. Making it so that when the cantilever is lowered it will interact with the tuning fork. A simple scheme of this set up is shown in Figure 5.6.

Using the lock-in an excitation signal was generated and inputted on the axis of the

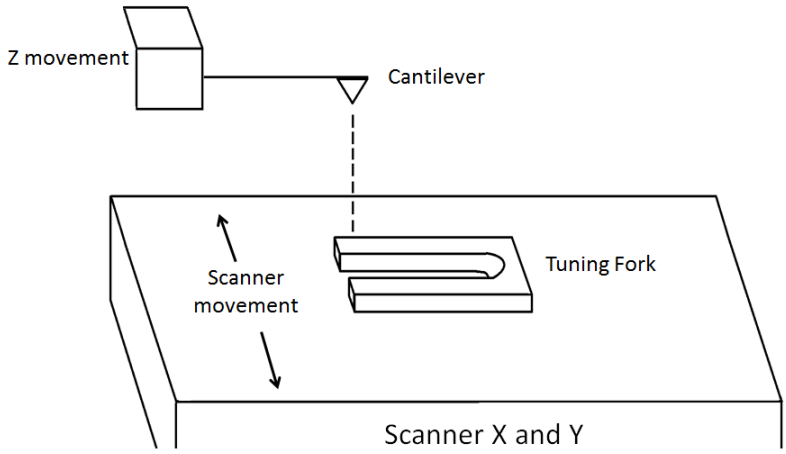

Figure 5.6: Simple schematic of the experiment set up.

scanner that was perpendicular to the sensor. After that, the tuning fork was excited near its resonance frequency and the control loop for the Z axis turned on, so that the cantilever could be lowered without crashing it against the tuning fork. Several force curves were acquired, giving the amplitude and phase measurement during approach and contact. This protocol was then repeated with the only variant being the frequency of the excitation signal that the scanner was applying. These frequencies were still close enough to the resonance frequency so that the amplitude of oscillation was still significant. Figure 5.7 presents a graph with the amplitude data of six different approach curves. There were many approach curves made for each excitation frequency, in the graph an extra curve for the frequency 35732Hz and 35802Hz were added, and although they don't perfectly overlap, they are still very similar and the data of the phase presented the same concept. It is also relevant to note that the frequencies are higher than the usual 32768Hz which is the resonance frequency of the tuning forks used in this work, because this tuning fork had one of its beams shortened which increased its resonance frequency.

As expected, once the cantilever enters contact with the tuning fork the amplitude starts going to zero. Using equations 4.4 and 4.5 presented in section 4.1, we can now determine the spring constant and damping coefficient of the interaction between the oscillating tuning fork and the static cantilever. The result of K_i, is presented in Figure 5.8 and the graph should be analysed from the right to the left, which represents the shortening distance between the two objects.

A lot of data calibration and calculations were required to achieve the result so it was a good way of knowing if there were any glaring mistakes. We know that before being close to each other the interaction between the oscillator and the cantilever should be very small or null, meaning that if the K_i presented high values before contact there was probably some error made during data calibration.

Although the constant spring of the interaction might be similar across different frequencies, the damping coefficient presented in Figure 5.9, is another matter entirely.

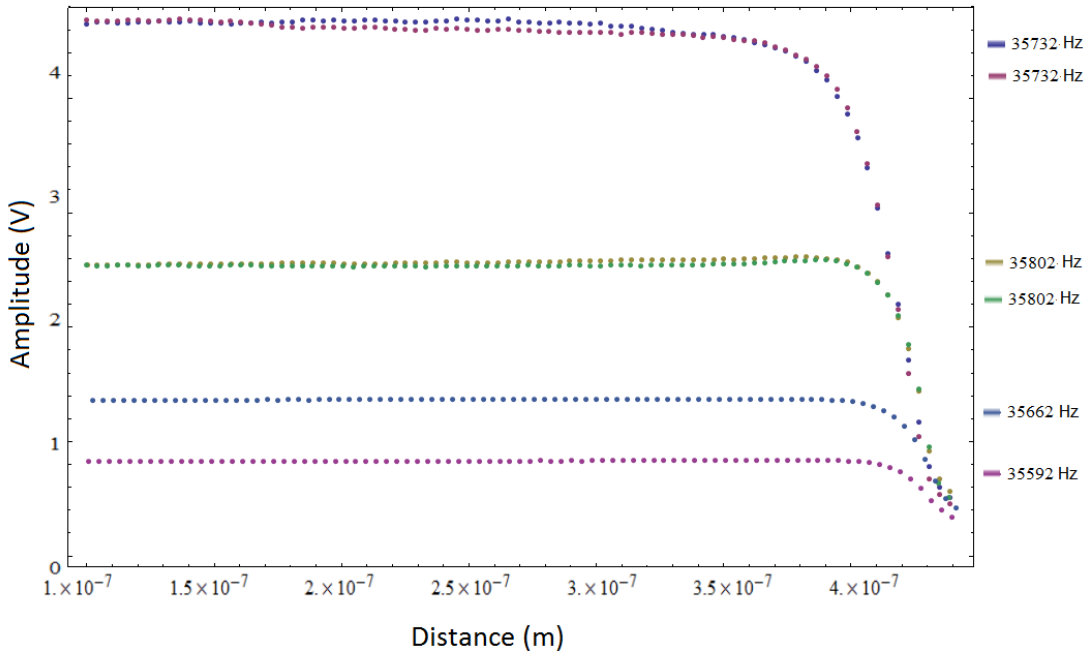

Figure 5.7: Amplitude of the tuning fork during cantilever approach.

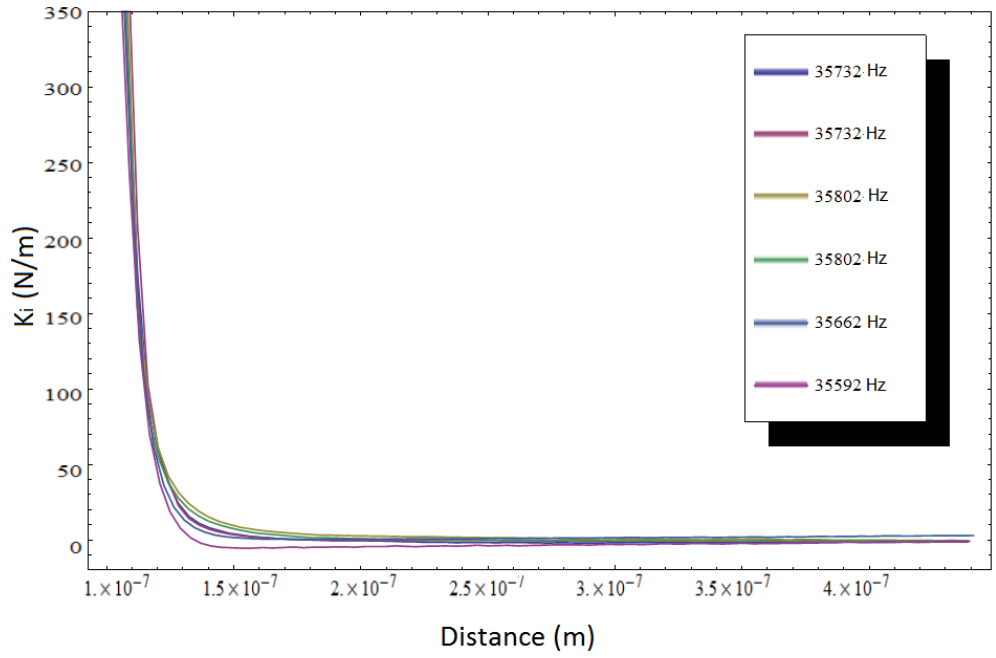

Figure 5.8: The interaction constant spring between the oscillating tuning fork and the static cantilever.

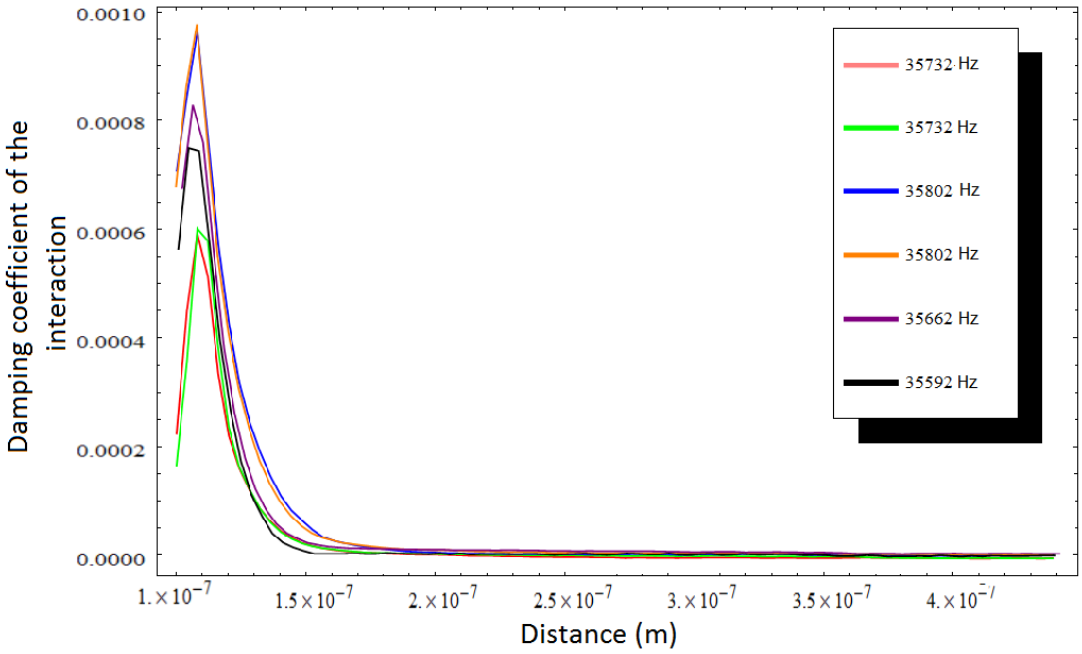

Figure 5.9: The damping coefficient of the interaction between the oscillating tuning fork and the static cantilever, with the lower two curves corresponding to 35732Hz frequencies.

As soon as the cantilever enters contact with one of the tuning forks moving beams a sliding friction force will take place, it is possible that the friction at this scale does not behave like the friction at a large scale. Either way what would be expected in first analysis, would be that the higher the amplitude movement of the tuning fork, the larger the area in which the friction force would be exercised. In this dissertation, we will not get into the study of friction forces at the nano scale level, the results are promising but more data is necessary to enter a discussion about nano scale friction. This experiment was meant to evaluate the stability of the microscope, its performance when measuring force-distance curves, test this methodology for the study of friction at the nano scale and to show there are a lot of possible uses for an AFM with a tuning fork.

5.4 Using genetic algorithm to optimize parameters

Across this work, the genetic algorithm was used more than once, this algorithm is a useful engineering tool and provides an efficient way of fitting or determining parameters under certain conditions. Since it was used it will be briefly explained and then its use in this work will be discussed.

The genetic algorithm in computer science uses a similar logic to nature's evolutionary processes [58], and it has seen a lot of use and evolution over the years, with some of its new iterations having a high impact in the scientific community [59]. Generally speaking,

the algorithm starts with a population of values that will be put through a test, which in the case of section 5.2 will be the contact mechanics models. Then, the values which presented less quadratic error (theoretical parameters producing a better fit), remain while the others are discarded, process that is called Selection. The survivors will then participate in the Crossover process where their characteristics are passed on to a new generation of values, however the Crossover is not perfect and there are slight Mutations. These mutations add variability to the algorithm and allow for better parameters to be generated, and then a new cycle starts, repeating over and over until the user interrupts the process or the minimal error is found. When trying to optimize the fitting of a function it is worth comparing this algorithm to a cycle that tries every possible value and chooses the one that minimizes the quadratic error, in this case the second option guarantees the best outcome, however like in section 5.3, where there were four parameters that required fitting, each of them with thousands of possible values, the number of possible combinations within these values were to high for the computer to calculate the quadratic error of each one of them in practical time. Which is why algorithms that fit functions, such as the fitting function of *Mathematica*, and the one made here that uses the genetic algorithm are so useful.

The source code of the program made in *Netlogo* to use this algorithm, as well as its interface, is presented in Annex III and Figure 5.10, shows the *Behavior Search* working in conjunction with the program to optimize the parameters.

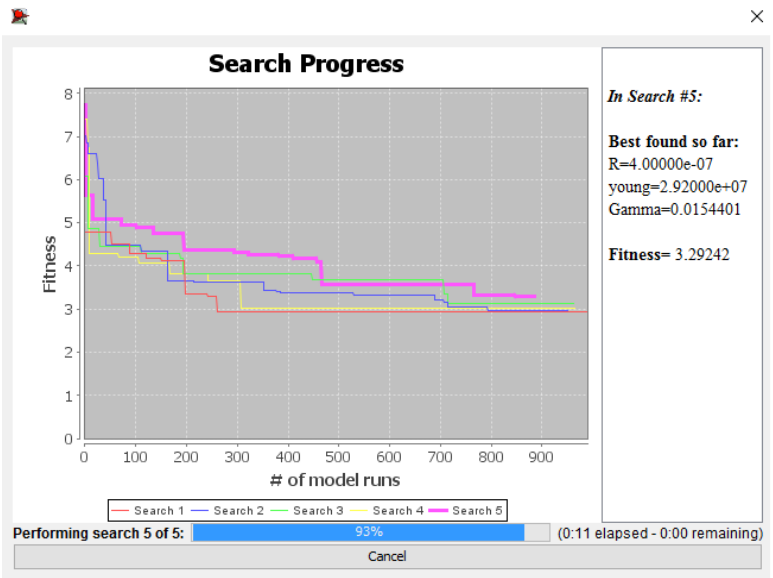

Figure 5.10: Interface of the behavior search software used, while optimizing parameters.

Chapter 6

Conclusions

An AFM using a tuning fork as a sensor was developed using very small resources. This AFM was then tested through making topography of known samples and by acquiring the Young's modulus of fairly known samples. A way to calibrate a scanner using a tuning fork was reported and other ways to utilize the versatility of the tuning fork were shown.

After making a theoretical review of the physics involved in Atomic Force Microscopy several sensors were considered and studied so that the best to perform AFM could be chosen.

This work required a lot of learning to operate different software such as the CAD program to designed the pieces of the AFM, something that required extensive attention to details. The *Mathematica* was also used for data processing, and to solve differential equations to apply the Euler-Bernoulli theory in the scanner. Electronics software was also used in *LTSpice*, for the design and test of circuits. Finally the use of *Netlogo* allowed to make custom programs for data processing, function fitting, or even the simulation of a Lock-In basic operations.

To finalize tallying the work developed, there was also a tip production set up made, which successfully was used to produce sharp tips. As an overall consideration, the built AFM was able to make topography of a calibration sample and a CD's tracks with bits, it is possible to conclude that the scanner made from a polymer material (which is very unusual for a scanner) works and that the AFM is functional. Seeing that the AFM was also used to determine correctly the samples Young's modulus, it shows that the tuning fork and AFM can be used to study mechanical properties of materials. However, it is important to note that the capacity of imaging surfaces is not at the same level of a commercial AFM. This is due to a number of factors some of each have a straight forward solution in future work done to optimize the AFM, such as an overall electromagnetic, mechanic and sound isolation system that can come in the form of a box for the AFM.

In conclusion, this work shows that with further development a very low-cost AFM (under 7000 euros), with equally cheap sensors, might be able to equal or surpass in proficiency an expensive commercial AFM (cost over 110 000 euros), and that the tuning forks can have several creative uses.

Bibliography

[1] M. Gauthier and S. Régnier. *Robotic micro-assembly*. John Wiley & Sons, 2011.

[2] J. C. Acosta, J. Polesel-Maris, F. Thoyer, H. Xie, S. Haliyo, and S. Régnier. "Gentle and fast atomic force microscopy with a piezoelectric scanning probe for nanorobotics applications". In: *Nanotechnology* 24.6 (2013), p. 065502.

[3] F. Pillet, L. Chopinet, C. Formosa, and É. Dague. "Atomic force microscopy and pharmacology: from microbiology to cancerology". In: *Biochimica et Biophysica Acta (BBA)-General Subjects* 1840.3 (2014), pp. 1028–1050.

[4] O. de Vegt, H. Vromans, J. den Toonder, and K. van der Voort Maarschalk. "Influence of flaws and crystal properties on particle fracture in a jet mill". In: *Powder Technology* 191.1 (2009), pp. 72–77.

[5] L. Taylor, D. Papadopoulos, P. Dunn, A. Bentham, N. Dawson, J. Mitchell, and M. Snowden. "Predictive milling of pharmaceutical materials using nanoindentation of single crystals". In: *Organic process research & development* 8.4 (2004), pp. 674–679.

[6] O. Guillaume-Gentil, E. Potthoff, D. Ossola, C. M. Franz, T. Zambelli, and J. A. Vorholt. "Force-controlled manipulation of single cells: from AFM to FluidFM". In: *Trends in biotechnology* 32.7 (2014), pp. 381–388.

[7] Q. Liu, T. Tong, S. Liu, D. Yang, and Q. Yu. "Investigation of using hybrid recycled powder from demolished concrete solids and clay bricks as a pozzolanic supplement for cement". In: *Construction and Building Materials* 73 (2014), pp. 754–763.

[8] A. Sharif. "Review on advances in nanoscale microscopy in cement research". In: *Micron* 80 (2016), pp. 45–58.

[9] B. Pittenger, N. Erina, and C. Su. "Quantitative mechanical property mapping at the nanoscale with PeakForce QNM". In: *Application Note Veeco Instruments Inc* (2010), pp. 1–12.

[10] A. Raman, S Trigueros, A Cartagena, A. Stevenson, M Susilo, E Nauman, and S. A. Contera. "Mapping nanomechanical properties of live cells using multi-harmonic atomic force microscopy". In: *Nature nanotechnology* 6.12 (2011), pp. 809–814.

[11] K. Sweers, K. van der Werf, M. Bennink, and V. Subramaniam. "Nanomechanical properties of α-synuclein amyloid fibrils: a comparative study by nanoindentation, harmonic force microscopy, and Peakforce QNM". In: *Nanoscale research letters* 6.1 (2011), p. 1.

[12] J. Adamcik, J.-M. Jung, J. Flakowski, P. De Los Rios, G. Dietler, and R. Mezzenga. "Understanding amyloid aggregation by statistical analysis of atomic force microscopy images". In: *Nature nanotechnology* 5.6 (2010), pp. 423–428.

[13] F. J. Giessibl. "Forces and frequency shifts in atomic-resolution dynamic-force microscopy". In: *Physical Review B* 56.24 (1997), p. 16010.

[14] A. in Motion LLC. *Atoms in Motion Chapter5*. http://atomsinmotion.com/book/chapter5/md. 2017 (accessed Jannuary 21, 2017).

[15] E. Charlaix and M. Ciccotti. "Capillary condensation in confined media". In: *arXiv preprint arXiv:0910.4626* (2009).

[16] G. Yang and R. Liu. "Viscosity Effect On The AFM Force Measurement". In: *Biophysical Journal* 96.3 (2009), 397a.

[17] P. Systems. *Basic Topographic Imagingn*. http://www.parkafm.com/index.php/park-spm-modes/91-standard-imaging-mode/223-basic-contact-afm-dynamic-force-microscope-dfm. 2017 (accessed Jannuary 23, 2017).

[18] B. Corporation. *Phase Detection*. http://www.nanophys.kth.se/nanophys/facilities/nfl/afm/fast-scan/bruker-help/Content. 2013 (accessed May 14, 2017).

[19] H. Edwards, L. Taylor, W. Duncan, and A. J. Melmed. "Fast, high-resolution atomic force microscopy using a quartz tuning fork as actuator and sensor". In: *Journal of applied physics* 82.3 (1997), pp. 980–984.

[20] W. Rensen, N. Van Hulst, A. Ruiter, and P. West. "Atomic steps with tuning-fork-based noncontact atomic force microscopy". In: *Applied Physics Letters* 75.11 (1999), pp. 1640–1642.

[21] M. Heyde, M. Kulawik, H.-P. Rust, and H.-J. Freund. "Double quartz tuning fork sensor for low temperature atomic force and scanning tunneling microscopy". In: *Review of scientific instruments* 75.7 (2004), pp. 2446–2450.

[22] N. Pavliček, B. Schuler, S. Collazos, N. Moll, D. Pérez, E. Guitián, G. Meyer, D. Peña, and L. Gross. "On-surface generation and imaging of arynes by atomic force microscopy". In: *Nature chemistry* 7.8 (2015), pp. 623–628.

[23] T. Ando, T. Uchihashi, N. Kodera, D. Yamamoto, A. Miyagi, M. Taniguchi, and H. Yamashita. "High-speed AFM and nano-visualization of biomolecular processes". In: *Pflügers Archiv-European Journal of Physiology* 456.1 (2008), pp. 211–225.

[24] F. J. Giessibl. "Atomic resolution on Si (111)-(7× 7) by noncontact atomic force microscopy with a force sensor based on a quartz tuning fork". In: *Applied Physics Letters* 76.11 (2000), pp. 1470–1472.

[25] F. J. Giessibl, F. Pielmeier, T. Eguchi, T. An, and Y. Hasegawa. "Comparison of force sensors for atomic force microscopy based on quartz tuning forks and length-extensional resonators". In: *Physical Review B* 84.12 (2011), p. 125409.

[26] M Gad, A. ITOH, and A. IKAI. "Mapping cell wall polysaccharides of living microbial cells using atomic force microscopy". In: *Cell biology international* 21.11 (1997), pp. 697–706.

[27] W. F. Heinz and J. H. Hoh. "Spatially resolved force spectroscopy of biological surfaces using the atomic force microscope". In: *Trends in biotechnology* 17.4 (1999), pp. 143–150.

[28] M. Szymonski, M. Targosz-Korecka, and K. E. Malek-Zietek. "Nano-mechanical model of endothelial dysfunction for AFM-based diagnostics at the cellular level". In: *Pharmacological Reports* 67.4 (2015), pp. 728–735.

[29] T. G. Kuznetsova, M. N. Starodubtseva, N. I. Yegorenkov, S. A. Chizhik, and R. I. Zhdanov. "Atomic force microscopy probing of cell elasticity". In: *Micron* 38.8 (2007), pp. 824–833.

[30] R. Garcia and E. T. Herruzo. "The emergence of multifrequency force microscopy". In: *Nature nanotechnology* 7.4 (2012), pp. 217–226.

[31] S. B. Kaemmer. *Introduction to Bruker's ScanAsyst and PeakForce Tapping AFM Technology*. 2011. URL: https://www.bruker.com/fileadmin/user_upload/8-PDF-Docs/SurfaceAnalysis/AFM/ApplicationNotes/Introduction_to_Brukers_ScanAsyst_and_PeakForce_Tapping_Atomic_Force_Microscopy_Technology_AFM_AN133.pdf (visited on 01/24/2017).

[32] B. Pittenger. *Introduction to Bruker's ScanAsyst and PeakForce Tapping AFM Technology*. 2015. URL: http://www.nanophys.kth.se/nanophys/facilities/nfl/afm/peak-force-calibr.pdf (visited on 01/24/2017).

[33] C. J. Chen. *Introduction to scanning tunneling microscopy*. Vol. 4. Oxford University Press on Demand, 1993.

[34] A. Castellanos-Gomez, N. Agraït, and G. Rubio-Bollinger. "Dynamics of quartz tuning fork force sensors used in scanning probe microscopy". In: *Nanotechnology* 20.21 (2009), p. 215502.

[35] G. H. Simon, M. Heyde, and H.-P. Rust. "Recipes for cantilever parameter determination in dynamic force spectroscopy: spring constant and amplitude". In: *Nanotechnology* 18.25 (2007), p. 255503.

[36] L. González, R. Oria, L. Botaya, M. Puig-Vidal, and J. Otero. "Determination of the static spring constant of electrically-driven quartz tuning forks with two freely oscillating prongs". In: *Nanotechnology* 26.5 (2015), p. 055501.

[37] J. Cleveland, S Manne, D Bocek, and P. Hansma. "A nondestructive method for determining the spring constant of cantilevers for scanning force microscopy". In: *Review of Scientific Instruments* 64.2 (1993), pp. 403–405.

[38] F. M. GmbH. *Femto HQA-15M-10T*. http://www.femto.de/images/pdf-dokumente/de-hqa-15m-10t_r3.pdf. 2010 (accessed May 23, 2017).

[39] A. J. Melmed. "The art and science and other aspects of making sharp tips". In: *Journal of Vacuum Science & Technology B: Microelectronics and Nanometer Structures Processing, Measurement, and Phenomena* 9.2 (1991), pp. 601–608.

[40] M. Kulawik, M. Nowicki, G. Thielsch, L. Cramer, H.-P. Rust, H.-J. Freund, T. P. Pearl, and P. S. Weiss. "A double lamellae dropoff etching procedure for tungsten tips attached to tuning fork atomic force microscopy/scanning tunneling microscopy sensors". In: *Review of scientific instruments* 74.2 (2003), pp. 1027–1030.

[41] M. A. Paul. *Electronic Principles, NY*. 1983.

[42] E. Margan. *Transimpedance Amplifier Analysis*. http://www-f9.ijs.si/~margan/Articles/trans_z_amplifier.pdf. 2012 (accessed June 21, 2017).

[43] K. D. Maria Persson Gulda. *Contact Mechanics*. imechanica.org/files/Contact%20Mechanics.ppt. 2008 (accessed April 27, 2017).

[44] D Fuard, T Tzvetkova-Chevolleau, S Decossas, P. Tracqui, and P Schiavone. "Optimization of poly-di-methyl-siloxane (PDMS) substrates for studying cellular adhesion and motility". In: *Microelectronic Engineering* 85.5 (2008), pp. 1289–1293.

[45] R. N. Palchesko, L. Zhang, Y. Sun, and A. W. Feinberg. "Development of polydimethylsiloxane substrates with tunable elastic modulus to study cell mechanobiology in muscle and nerve". In: *PloS one* 7.12 (2012), e51499.

[46] A. Groisman, M. Enzelberger, and S. R. Quake. "Microfluidic memory and control devices". In: *Science* 300.5621 (2003), pp. 955–958.

[47] F. Schneider, T Fellner, J Wilde, and U Wallrabe. "Mechanical properties of silicones for MEMS". In: *Journal of Micromechanics and Microengineering* 18.6 (2008), p. 065008.

[48] K. Johnson, K Kendall, and A. Roberts. "Surface energy and the contact of elastic solids". In: *Proceedings of the Royal Society of London A: Mathematical, Physical and Engineering Sciences*. Vol. 324. 1558. The Royal Society. 1971, pp. 301–313.

[49] B. Derjaguin, V. Muller, and Y. P. Toporov. "Effect of contact deformations on the adhesion of particles". In: *Progress in Surface Science* 45.1-4 (1994), pp. 131–143.

[50] E. Barthel. "Adhesive elastic contacts: JKR and more". In: *Journal of Physics D: Applied Physics* 41.16 (2008), p. 163001.

[51] X. Zhu. *Tutorial on Hertz Contact Stress*. https://wp.optics.arizona.edu/optomech/wp-content/uploads/sites/53/2016/10/OPTI-521-Tutorial-on-Hertz-contact-stress-Xiaoyin-Zhu.pdf. 2012.

[52] M. Liu, J. Sun, and Q. Chen. "Influences of heating temperature on mechanical properties of polydimethylsiloxane". In: *Sensors and Actuators A: Physical* 151.1 (2009), pp. 42–45.

[53] I. Johnston, D. McCluskey, C. Tan, and M. Tracey. "Mechanical characterization of bulk Sylgard 184 for microfluidics and microengineering". In: *Journal of Micromechanics and Microengineering* 24.3 (2014), p. 035017.

[54] F. Rahman. *Nanostructures in Electronics and Photonics*. Pan Stanford Publishing Pte. Ltd, 2008.

[55] S. Landis. *Nano Lithography*. Wiley-ISTE, 2011.

[56] W. Zhou. *Nanoimprint Lithography, An Enabling Process for Nanofabrication*. Springer, 2013.

[57] G. Marchesi, C. O. Navarra, M. Cadenaro, M. R. Carrilho, B. Codan, V. Sergo, R. Di Lenarda, and L. Breschi. "The effect of ageing on the elastic modulus and degree of conversion of two multistep adhesive systems". In: *European journal of oral sciences* 118.3 (2010), pp. 304–310.

[58] D. Whitley. "A genetic algorithm tutorial". In: *Statistics and computing* 4.2 (1994), pp. 65–85.

[59] K. Deb, A. Pratap, S. Agarwal, and T. Meyarivan. "A fast and elitist multiobjective genetic algorithm: NSGA-II". In: *IEEE transactions on evolutionary computation* 6.2 (2002), pp. 182–197.

Appendix

Appendix 1 Technical Designs

These designs were made to order the pieces from external sources, however, in the end the top plate ended up being 3D printed by the company *ShapeWays*, the spacer was build in the lab using two blocks of wood, and the bottom plate was also manually built in the lab using a plywood board. These drawings show some of the technical requirements that had to be carefully planned.

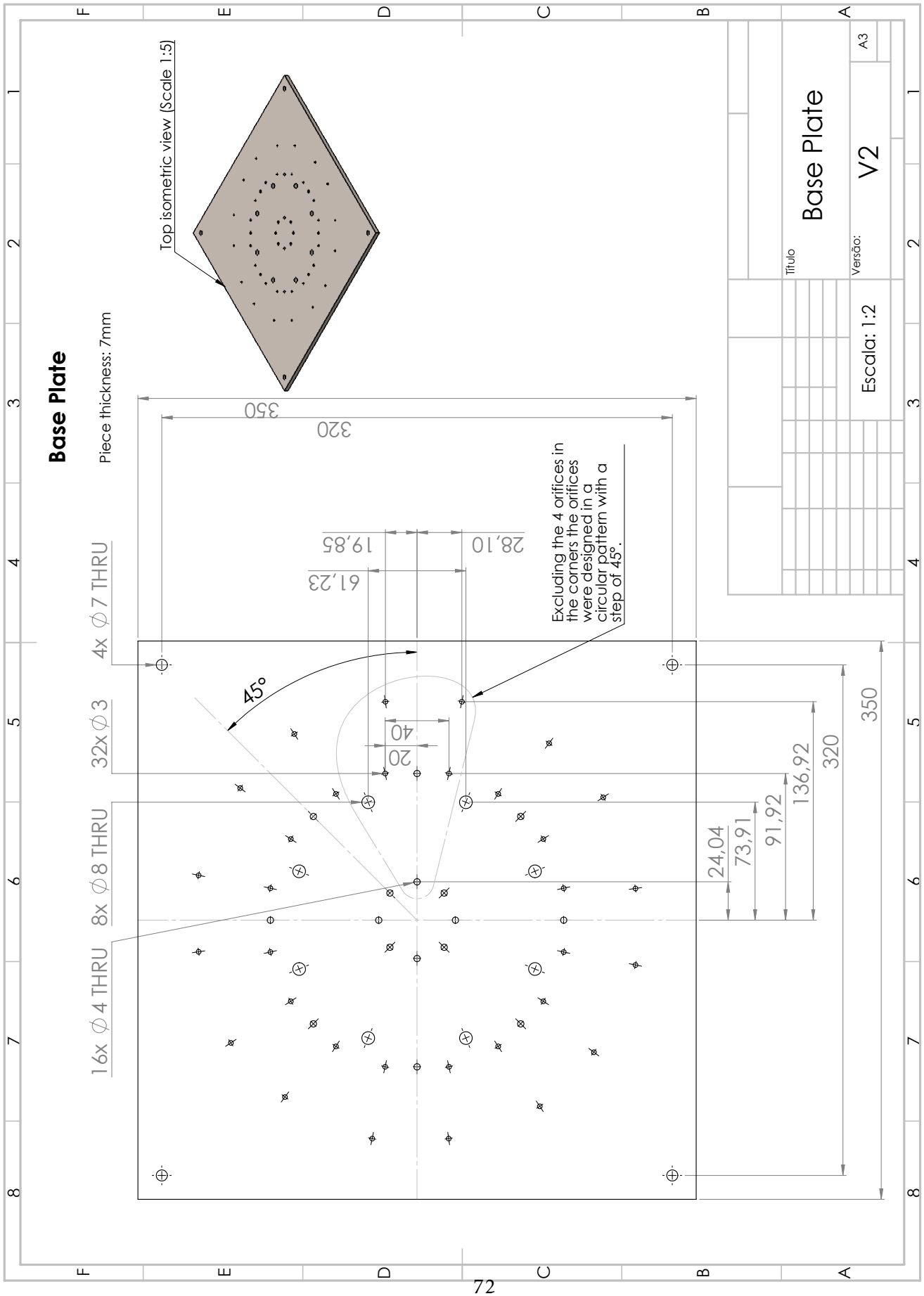

Figure A.1: Technical design of the base plate for the AFM.

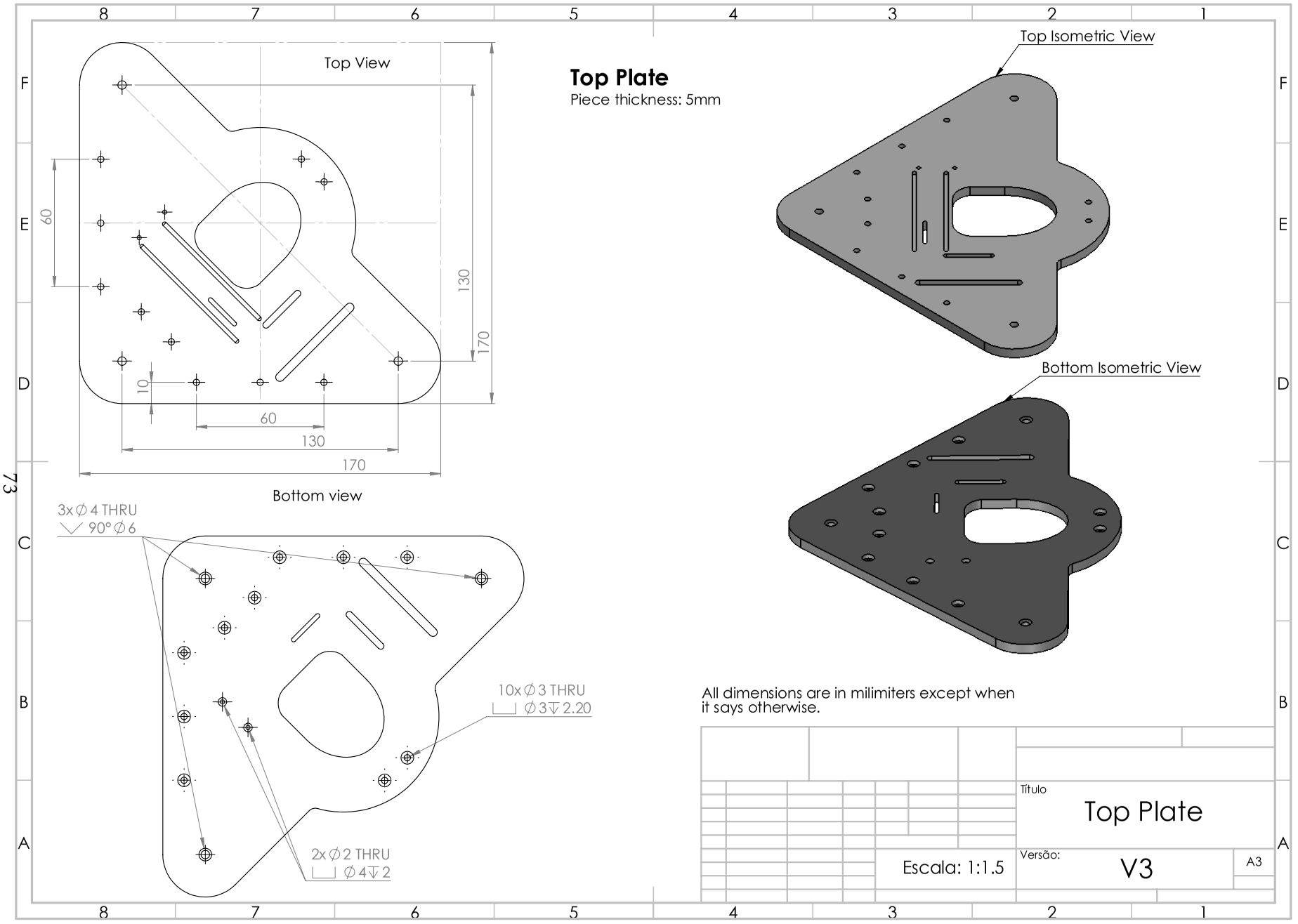

Figure A.2: Technical design of the top plate for the AFM.

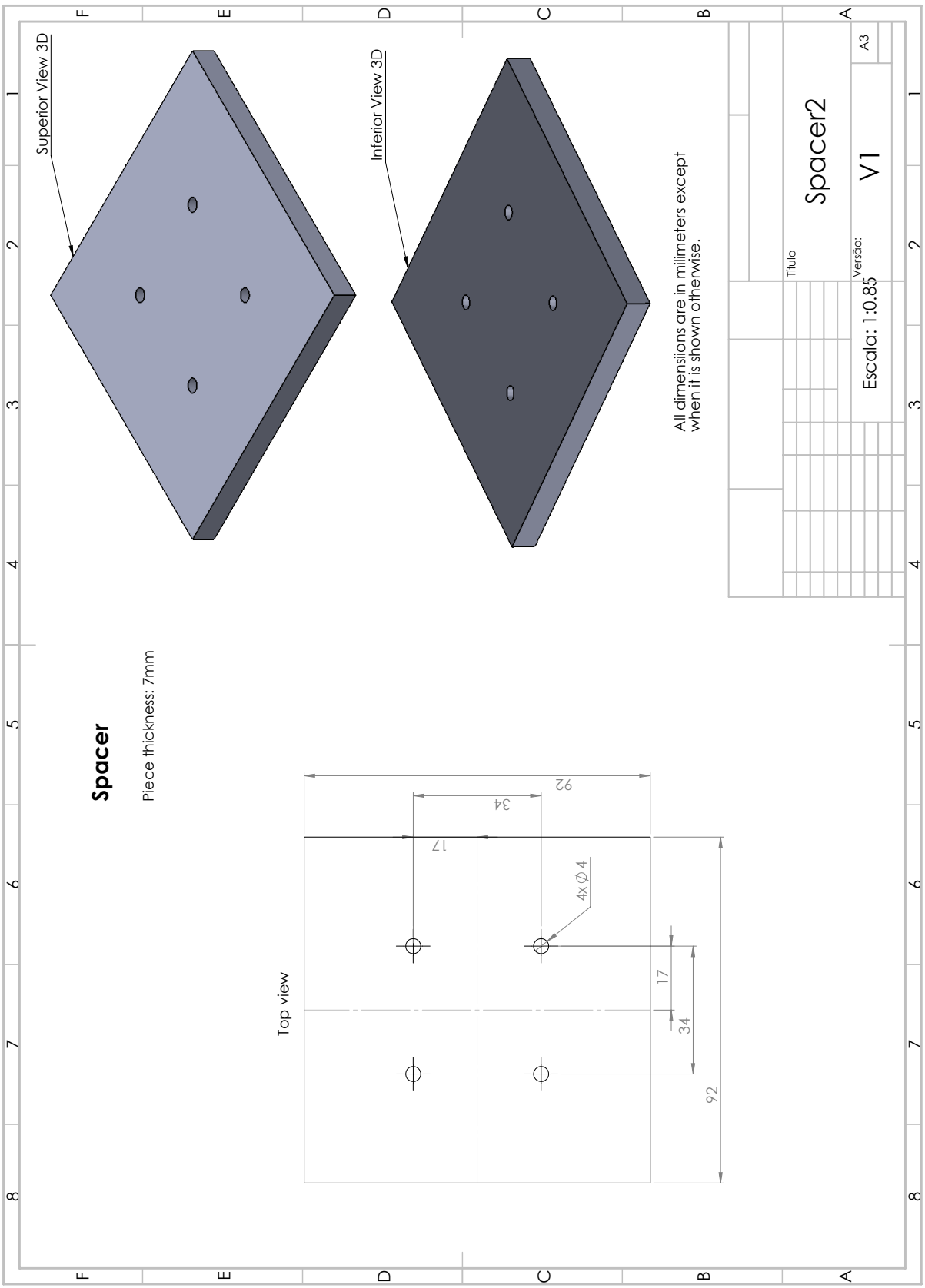

Figure A.3: Technical design of the spacer between the base plate and the micro-metric table for the AFM.

APPENDIX B

Appendix 2 Fitting Data Program

This annex presents the program made in *Netlogo* that used in conjunction with *Behavior Search* allowed to fit the experimental data, using a genetic algorithm and the contact mechanics models.

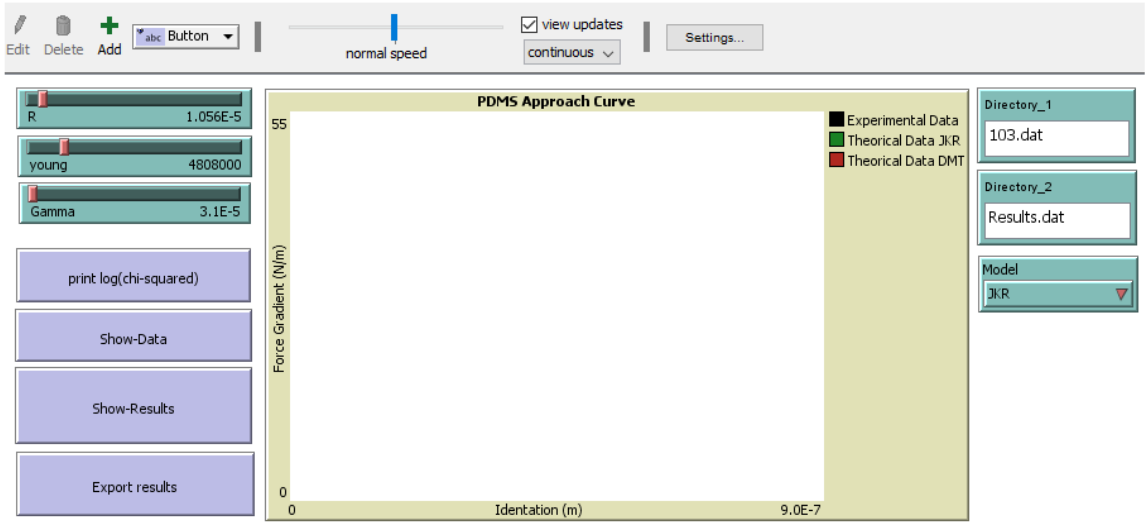

Figure B.1: Interface of the program made in *Netlogo* to use the genetic algorithm.

The source code of the program made.

```
1
2  Globals[
3    X-Value          ; Variables that take on the values of the points in the graph
4    Y-Value
5    A-Value
6    B-Value
7    C-Value
```

```
  chisquared2    ;Second variable of error
  ListA
  ]

Extensions [table]

to-report Chi_squared                ;Function that calculates the total error
  let chisquared 0

  file-open Directory_1
    while [ not file-at-end?] [
     set chisquared2 chisquared2 + ( theoretic-model file-read file-read) ^ 2
;Calculation of the error
    ]
  file-close

  report log chisquared2 10 ;Logarithmic representation of the error
end

to-report theoretic-model [Delta Y]  ;Calculates value based on model chosen

  if Model = "DMT" [ report Y - 2 * young * Sqrt(Delta) * Sqrt(R) ]
  if Model = "JKR" [ report Y + ((3 * Sqrt(Pi) * Sqrt(R) * Sqrt(young) *
  Sqrt(Gamma) * (R * Delta)^(1 / 4)) / (Sqrt(Delta))) - 2 * young *
  Sqrt(R * Delta) ]

end

to execute
  print Chi_squared     ;Shows the error
end

to Show-Results         ;Function that presents the results in graph form on
            the interface
  clear-all
  reset-ticks
  set X-Value 0
  set Y-Value 0
  set A-Value 0
  set B-Value 0
  set ListA []

  file-close
  file-open Directory_1
  while [not file-at-end?] [
  set X-Value file-read
  set Y-Value file-read
  set A-Value X-Value
  let Delti A-Value
  set B-Value ((3 * Sqrt(Pi) * Sqrt(R) * Sqrt(young) * Sqrt(Gamma) *
```

```
  ((R * Delti) ^ (1 / 4))) / Sqrt(Delti)) + 2 * young * Sqrt(R * Delti)
  set C-Value 2 * young * Sqrt(Delti) * Sqrt(R)
  set ListA lput C-Value ListA
  tick]
  file-close
end

to show-data            ;Function that shows experimental data in graph
  reset-ticks

  file-close
  file-open Directory_1
  while [not file-at-end?] [
  set Y-Value file-read
  set X-Value file-read
   tick]
  file-close
end

to Export-results      ;Function tha exports a file with the results
  let counter 0
  file-delete Directory_2
    file-open Directory_2

    while[counter < length listA][
      file-write item counter listA
      ;file-print "\n"
      set counter counter + 1]

    file-close
end
```